

Contents lists available at [ScienceDirect](https://www.sciencedirect.com)

International Journal of Plasticity

journal homepage: www.elsevier.com/locate/ijplas

Effect of Lüders and Portevin–Le Chatelier localization bands on plasticity and fracture of notched steel specimens studied by DIC and FE simulations

S.C. Ren, T.F. Morgeneyer^{*}, M. Mazière, S. Forest, G. Rousselier

MINES ParisTech, PSL University, MAT-Centre des Matériaux, CNRS UMR 7633, BP 87 91003, Evry, France

ARTICLE INFO

Keywords:

C–Mn steel
 Single edge notch tension
 High temperature DIC
 Portevin–Le Chatelier effect
 Strain localization
 Slant fracture

ABSTRACT

The impact of the Portevin–Le Chatelier (PLC) effect on plasticity and fracture ahead of a severe notch is investigated by DIC field measurements for C–Mn steel. The PLC effect causes an intermittent activity of highly localized strain rate bands. This first high temperature investigation of the effect of a notch on the PLC localization bands is successfully reproduced numerically in terms of strain localization in 3D FE simulations. This thereby validates quantitatively the McCormick-type model under these complex conditions. It is found that, when the PLC effect is at play at elevated temperature (175 °C), a flat to slant crack transition is observed. In contrast, at room temperature, when only Lüders bands are active, the crack remains mostly flat, i.e. normal to the loading direction of the SENT samples. This behaviour may be related to the early loss of symmetry and intermittency of the plastic zone that is found for PLC even affecting the initial Lüders bands at elevated temperature. During the slant fracture at high temperature, only half the fracture energy is absorbed compared to flat fracture at room temperature. The McCormick-type model simulations predict slant strain rate bands through the sample thickness, that are consistent with the slant fracture found at elevated temperature. Accordingly, no slant bands are found for simulations outside the PLC domain. Both experiments and simulations show PLC strain localization bands that are flip-flopping up and down during crack propagation. By combining the McCormick-type model with a Rousselier porous plasticity model, the flat fracture of the sample at room temperature and the associated macroscopic curve are reproduced successfully, but the toughness at elevated temperature is overestimated.

1. Introduction

The Portevin–Le Chatelier (PLC) effect has been widely observed in various industrial alloys over a certain range of temperatures and strain rates. It is usually revealed by the stress serrations (or ‘jerky flow’) and associated propagative localization bands of plastic strain rate at the macroscopic scale. The localized bands leave traces on the surface of material sheets during material forming (Grabner et al., 2019). A precise characterization of the PLC sensitive domain would be useful for eliminating these manufacturing defects. In addition, the degradation of certain mechanical properties has been considered to be related to strain ageing and the PLC effects, such as loss of toughness and ductility (Chakravarty et al., 1983; Amar and Pineau, 1985; Gomiero et al., 1992; Kim et al., 2004; Wang et al., 2012). The PLC effect is due to dynamic strain ageing (DSA) which is attributed, at the microscopic scale, to the pinning/unpinning of mobile dislocations by the diffusion of solute atoms (Cottrell and Bilby, 1949), though

^{*} Corresponding author.

E-mail address: thilo.morgeneyer@mines-paristech.fr (T.F. Morgeneyer).

<https://doi.org/10.1016/j.ijplas.2020.102880>

Received 11 May 2020; Received in revised form 12 October 2020

Available online 28 October 2020

0749-6419/© 2020 Elsevier Ltd. All rights reserved.

other mechanisms, such as pseudo PLC mechanism (Brechet and Estrin, 1996) and precipitate shearing (Chmelifk et al., 1998), may also be responsible. Different diffusion mechanisms have been proposed for different material systems. According to Cottrell and Bilby (1949), both interstitial and substitutional atoms can diffuse in the volume (bulk diffusion) to form a cloud of atoms (Cottrell atmosphere) around the dislocations. The strain ageing results from solute atoms being dragged along by the continuous movement of dislocations. van den Beukel (1975) later recognized that solute atoms do not have sufficient mobility to follow moving dislocations. The motion of mobile dislocations is an intermittent process, and the solute atoms diffuse to mobile dislocations temporarily arrested by obstacles such as forest dislocations. In addition to the basic bulk diffusion mechanism, Mulford and Kocks (1979) suggested that a simultaneously running pipe diffusion should be considered which denotes the enhanced line diffusion of atoms from the forest dislocations to the mobile dislocations during the waiting time of mobile dislocations. Curtin et al. (2006) introduced the “cross-core” theory which indicates an earlier local rapid diffusion inside the dislocation core. These findings suggest that the exponent of the solute concentration function needs to be revised (Epperly and Sills, 2020). The physical justifications for the cross-core theory were based on the Al–Mg system with substitutional atoms. In contrast, interstitial atoms can diffuse more freely in the bulk. The vacancy or dislocation line assisted diffusion may not be the dominating mechanism in an interstitial system. Detailed justifications of the diffusion mechanisms in different material systems may help to build more sophisticated and accurate models.

Strain ageing phenomena are ubiquitous in engineering alloys. For aluminium alloys like Al–Mg (Chihab et al., 1987; Clausen et al., 2004; Ait-Amokhtar et al., 2006; Halim et al., 2007) and Al–Cu (Ranc and Wagner, 2005; Böhlke et al., 2009), the PLC effect usually occurs at room temperature. For ferritic C–Mn steels (Wang et al., 2012; Ranc et al., 2016), it is observed at around 200 °C. It has also been reported in Nickel based superalloys around 500 °C (Dybiec and Chaturvedi, 1991; Rao et al., 1995; Fournier et al., 2001; Cai et al., 2017), and around 600 °C for Cobalt based superalloys (Chaboche et al., 2013; Mazière and Pujol d’Andrebo, 2015) as well as in Titanium alloys around 400 °C (Prasad and Varma, 2008; Marchenko et al., 2016).

Before the wide application of imaging techniques, such as digital image correlation (DIC) and digital image thermography (DIT), the identification of the PLC effect was usually based on the serrations observed on the stress–strain curves of uni-axial tensile tests. However, this method can cause ambiguities as it is sometimes hard to identify the small serrations from the measurement noise. Localization bands can occur with nearly invisible serrations (Ren et al., 2019). It is particularly important for the calibration of models to predict the critical strain of the onset of PLC effect (Mazière and Dierke, 2012). Non-contact field measurement methods reveal more details about the PLC effect with good accuracy (Bernard et al., 2006). In the literature, Al–Mg alloys are the most popular alloys for the study of the PLC effect because they exhibit intensive serrations at room temperature. The occurrence of the PLC effect at room temperature makes the experimental set-up less demanding. The band properties like width, propagation speed, carried strain/strain rate and their spatio-temporal evolution during smooth tensile testing have been investigated with DIC in many works (Tong et al., 2005; Ait-Amokhtar et al., 2006; Halim et al., 2007; Zdunek et al., 2008; Casarotto et al., 2009; Zavattieri et al., 2009; de Codes et al., 2011; Cheng et al., 2015; Klusemann et al., 2015; Cai et al., 2016; Yuzbekova et al., 2017). PLC bands have also been characterized by DIC in Al–Cu alloys via tensile tests at room temperature (Jiang et al., 2005; Zhang et al., 2005). DIC measurements of PLC effects in tension at high temperature have only been performed recently for Nickel based alloys by Swaminathan et al. (2015) and Cai et al. (2017). Besides, Ranc et al. (2016) observed the PLC effect in C–Mn steel tensile specimen at 200 °C with DIT.

Most real structures possess complex geometrical features such as holes and edges for design purposes and they may contain defects and flaws such as fatigue cracks. In the presence of a notch, the highly inhomogeneous strain gradient makes these sites more sensitive to the PLC effect. Even in uni-axial tensile tests, the localization bands are usually found to nucleate at the edge of the curved transition zone to the grip section due to strain gradients (Klusemann et al., 2015). In the literature on PLC measurements, less attention has been paid to other geometries than smooth tensile ones (Graff et al., 2004). Coër et al. (2013) studied the Lüders and PLC bands during simple shear test. Le Cam et al. (2017) showed the PLC bands during equi-biaxial tensile loading. The PLC band morphology is different under biaxial conditions compared to uniaxial conditions (Min et al., 2015). Concerning the compact tension (CT) specimens, only the Lüders bands have been observed by Belotteau et al. (2009), Wang et al. (2012) and Wenman and Chard-Tuckey (2010) at room temperature. However, many standard fracture toughness tests require notched specimens such as CT, SENT and SENB (single edge notched bending). A measurement of the band formation in those cases other than smooth tensile ones could be useful for validating numerical results as the interaction between the PLC effect and ductile tearing is unknown at present. As reported by Hickey and Ravi-Chandar (2016), two kinds of plastic strain localized zones that precede fracture were observed and resulted in different fracture modes for 6061 alloy with two different heat treatments. Recent observations by in-situ synchrotron X-ray laminography also reported slant intermittent localization bands at early loading stages ahead of the notch of 2xxx alloy CT-like specimens (Morgeneyer et al., 2014, 2016; Buljac et al., 2016, 2018). The damage events were found at the final stage of loading following the traces of localization bands. The bands measured by DIC may provide new insights for understanding fracture events. To the best of our knowledge, the present work is the first contribution that shows the PLC localization behaviour at notch tip measured at high temperature with DIC.

Based on the DSA theory, theoretical constitutive laws have been developed in order to model the PLC effect. A phenomenological model that uses the negative strain rate sensitivity (nSRS) to explain the serrations was proposed by Penning (1972) and Kubin and Estrin (1985) which is able to reproduce the main features of PLC effect such as serrations and localization (Benallal et al., 2006). Another macroscopic model (McCormick, 1988; Mesarovic, 1995; Zhang et al., 2001) is based on a time varying state variable namely the ageing time t_a which controls the mean local concentration of solute atoms at dislocations. This model originates from the physical DSA mechanisms at the scale of dislocations and has been validated by field measurement techniques (Benallal et al., 2008; Klusemann et al., 2015). A modified version has been implemented in the finite element code Zset (Graff et al., 2004, 2005,

Table 1
Chemical composition (wt%) of the A42 steel used for the current study.

C	N	Al	Si	P	S	V	Cr	Mn	Ni	Cu	Nb	Mo	Sn
0.15	0.004	0.019	0.19	0.034	0.021	< 0.002	0.034	0.73	0.05	0.041	< 0.002	0.006	0.003

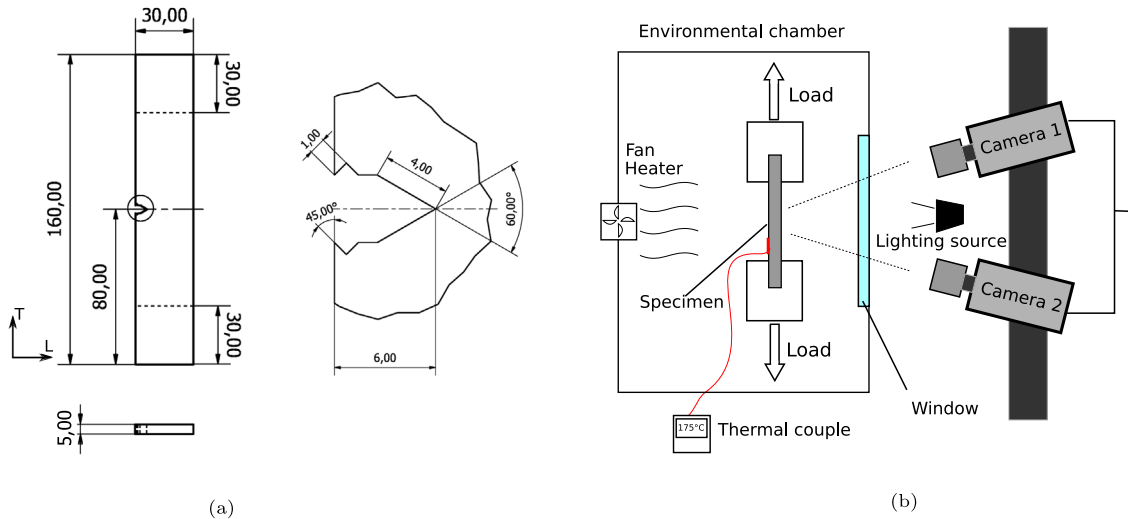


Fig. 1. (a) Geometry of the SENT specimen used in the present work (mm). The section clamped inside the grip is 30 mm long as marked by dashed lines. (b) DIC setup for high temperature test. The labels A, B, C and D are explained in Table 2.

2008; Mazière et al., 2010; Ren et al., 2017). In the present work, the McCormick approach will be used in the simulations based on its proven ability to describe localization bands in an accurate and efficient manner.

The aim of the current work is to investigate the kinematic and mechanical characteristics of PLC bands at notch before crack initiation and during crack propagation in order to better understand the effect of PLC on fracture. The chosen material has been tested at room temperature and low temperature (from -150°C to 0°C) by Marais et al. (2012). Wagner et al. (2006) and Huang et al. (2015) reported that the minimum nSRS and elongation were observed around 200°C for A42 steel. The temperature for characterizing the PLC effect is chosen to be 175°C which is in the nSRS domain.

The paper is organized as follows. The results of mechanical tests and DIC measurements at room temperature and 175°C are presented in Section 2. A comparison of the spatio-temporal behaviour of localization bands at these two temperatures is drawn. In Section 3, the formulation of the McCormick type model including the identification procedure is given. 3D finite element simulations are conducted in an attempt to reproduce the experimental observations. In Section 4, a discussion will be given on the experimental and numerical results especially on the flat and slant fracture modes observed at two temperatures.

2. Experimental results

2.1. C-Mn steel and specimen geometry

The investigated C-Mn steel (A42) is used for the secondary loop of pressurized water reactors (PWR) (Marais et al., 2012). The tubes made of this material are subjected to internal pressure ranging from 70 to 80 bar and temperatures from 0°C up to 280°C . The chemical composition of A42 steel can be found in Table 1.

The interstitial atoms such as carbon and nitrogen interact with mobile dislocations which play an important role in the strain ageing mechanism. Carbon is involved during the manufacturing process. The content of aluminium has been kept low to avoid the formation of aluminium nitrides (AlN), so that freely diffusing nitrogen remains in the crystalline lattice which also makes this steel sensitive to dynamic strain ageing.

The SENT specimens were prepared with a wire electrical discharge machine. The specimens contain round notches with 0.17 mm radius. The geometry is illustrated in Fig. 1(a). This sample geometry is chosen to assess the influence of the PLC effect on ductile tearing in a case where the entire ligament undergoes plastic deformation at the beginning of the test. These specimens were cut from a seamless pipe obtained by a circular rolling process with the longitudinal direction along the transverse direction (T). The microstructure is composed of ferrite and pearlite. The ferrite grain is equiaxed in the LS and TS plane with a size around $22\text{--}31\ \mu\text{m}$ (Marais et al., 2012).

Table 2
Summary of experimental conditions and main experimental observations.

	Loading rate (mm/s)	T (°C)	PLC (Yes/No)	Fracture mode
Specimen A	0.01	20	No	Flat
Specimen B	0.01	175	Yes	Slant
Specimen C	0.002	20	No	Flat
Specimen D	0.002	175	Yes	Slant

2.2. Mechanical tests for SENT specimens

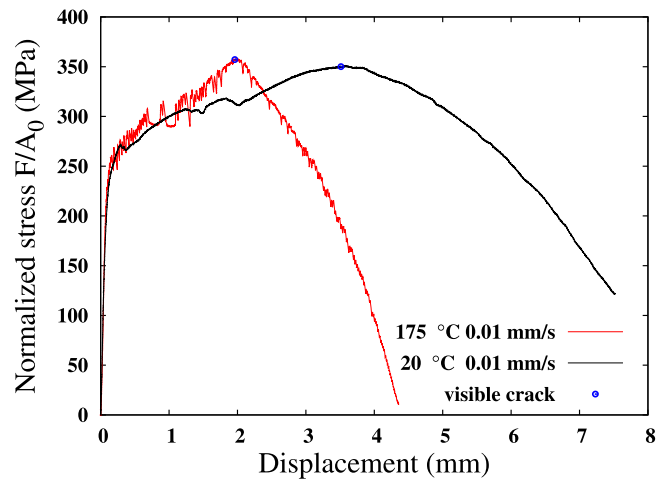
The mechanical behaviour of this material, especially the Lüders effect, has been investigated by Marais et al. (2012) under simple tension from -150°C to 20°C . The Lüders effect were observed over the whole temperature range on their tensile stress–strain curves. A similar C–Mn steel (TU48C) has been investigated by Belotteau (2009) and Wang et al. (2012) in the temperature range between 20°C and 350°C . The TU48C has been found to be very sensitive to the PLC effect between 150°C and 300°C . The current A42 steel is similar to TU48C, but it has a higher aluminium content. For this amount of aluminium, more nitrogen atoms are trapped as aluminium nitrides which make this alloy probably less sensitive to DSA. Huang et al. (2015) showed a minimum SRS at around 200°C for the A42 steel (their A42 steel contains higher Al than the received material tested which is supposed to be more sensitive). That is the reason for choosing 175°C to explore the possible PLC effect. The present study consists in comparing the mechanical behaviour, especially the localization bands around the notch area of these SENT specimens in the PLC sensitive domain and in the non-sensitive domain. Tests were carried out using a 100 kN MTS machine under displacement control. In order to perform high temperature tests and monitor the localization evolution, the tensile machine was combined with an environmental chamber and a DIC system (see Fig. 1(b)). A thermocouple was directly welded on the surface of the tested specimens for temperature control. Images were acquired through the furnace window. The four test conditions are summarized in Table 2. In this table, the existence of PLC effect and fracture mode associated with each specimen is also mentioned.

The variation of the normalized force, defined by F/S_0 (F : force; S_0 : initial notch plane section) as a function of the cross-head displacement is plotted in Fig. 2. Fig. 2(a) gives a comparison of the force–displacement curves at 175°C and room temperature with the same loading rate 0.01 mm/s . Serrations can be observed on the 175°C curve which is in the PLC sensitive domain. It can also be noticed that the ductility of the material is reduced by 40% at 175°C compared to its room temperature value. Similar phenomena were observed for the tests with a loading rate of 0.002 mm/s . In addition, the stress levels at these two loading rates are similar. The blue point marks the moment a visible crack was observed at the surface.

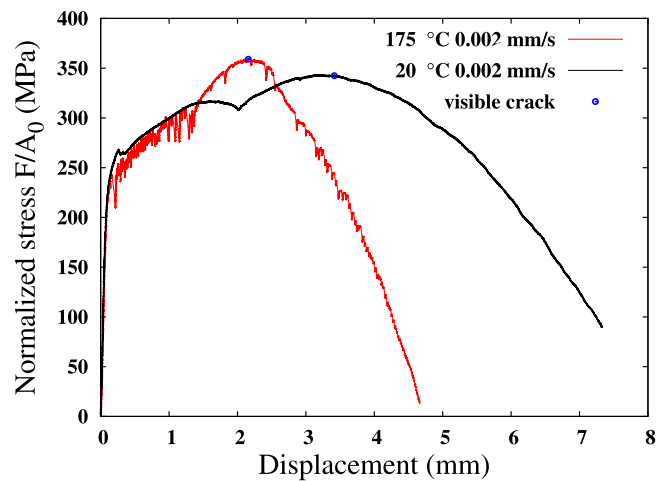
The tested SENT specimen has a larger front surface–thickness ratio compared to a standard specimen (e.g. BS 8571). These specimens are designed for observing the PLC effect with DIC measurements during crack propagation. Two distinct modes of crack can be observed in ductile plates: flat mode and flat-to-slant mode (Xue and Wierzbicki, 2009). Flat to slant crack transition can typically be observed in ductile thin sheet materials. The crack initiates perpendicularly to the loading direction from the notch and then turns to 45° with respect to the loading direction during crack propagation. We distinguish the crack initiation energy U_i from the crack propagation energy U_p as shown in Fig. 3. The total fracture energy is therefore $U_t = U_i + U_p$ (see also Dalloz, 2007; Buirette et al., 2014). As all the four tests were performed with the same specimen geometry, the fracture energy could be considered as an indicator for comparing the toughness. Fig. 3 shows the fracture energy for specimens tested under different conditions. The fracture energy at room temperature is much higher than that at 175°C with a factor ranging from 1.72 to 2. In contrast, the energy partition is similar at both temperatures.

2.3. High temperature DIC setup

For the DIC measurement, a stereo-DIC system using two Manta G-419B cameras (2048×2048 pixels each) with Schneider Xenoplan 2.8/50 M30.5 lenses was synchronized with the tensile machine. LED light sources were placed along the middle line between the two cameras. The most important issue for a successful high temperature DIC measurement is to obtain a contrast pattern resistant to temperature change. A coating of high temperature resistant (up to 700°C) black paint was sprayed onto the specimen which forms a uniform background colour layer to avoid oxidation. A random white speckle pattern was then sprayed onto the black surface. For the specimens tested at room temperature, ordinary white paint was used as the background colour layer. Black speckle was then sprayed onto the white surface. The accuracy of DIC measurement of strain fields can be reduced by convection air flow that can cause variations in the refractive index at elevated temperatures. The measurement noise of strain along the loading axis ϵ_{yy} was examined before testing by analysing images taken from undeformed specimens that is similar to Min et al. (2016). The standard deviation of measurement noise (ϵ_{yy}) was 0.000294 at 175°C compared to 0.000089 at room temperature. To obtain a reliable measurement, the incremental strain carried inside a localization band should be higher than the measurement noise. A sufficient time interval was chosen between the reference and the deformed image (see Section 2.4). As shown in Figs. 4–7, the maximum strain scale is fixed at 0.003 which is 10 times larger than the measurement noise. The real strain increment used for calculating the strain rate inside a localization band is much higher than the measured noise. As shown in Fig. 9(a), when $\dot{\epsilon}_{yy}$ reaches 0.0012 s^{-1} for specimen A, the strain increment is 0.024 (the time interval between the reference and the current image is 20 s) which is 269 times larger than the measurement noise. Similarly, as shown in Fig. 9(b) for specimen B, when $\dot{\epsilon}_{yy}$ reaches 0.0020 s^{-1} the strain increment is 0.04 which is 136 times larger than the measured noise.



(a) Specimen A and B



(b) Specimen C and D

Fig. 2. The variation of nominal stress against cross-head displacement for the 4 tests under different test conditions. (a) A comparison of the two tests at 175 °C and 20 °C for the same loading rate 0.01 mm/s. (b) The two tests with a loading of rate 0.002 mm/s.

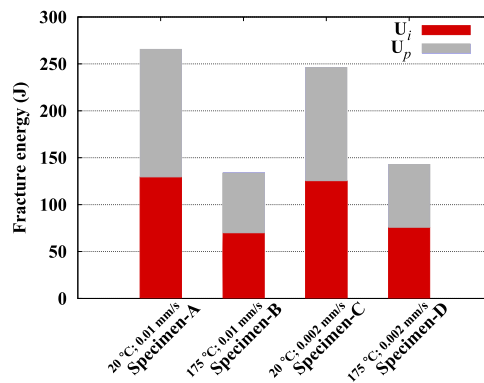
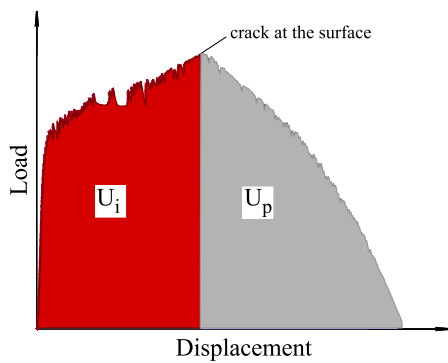
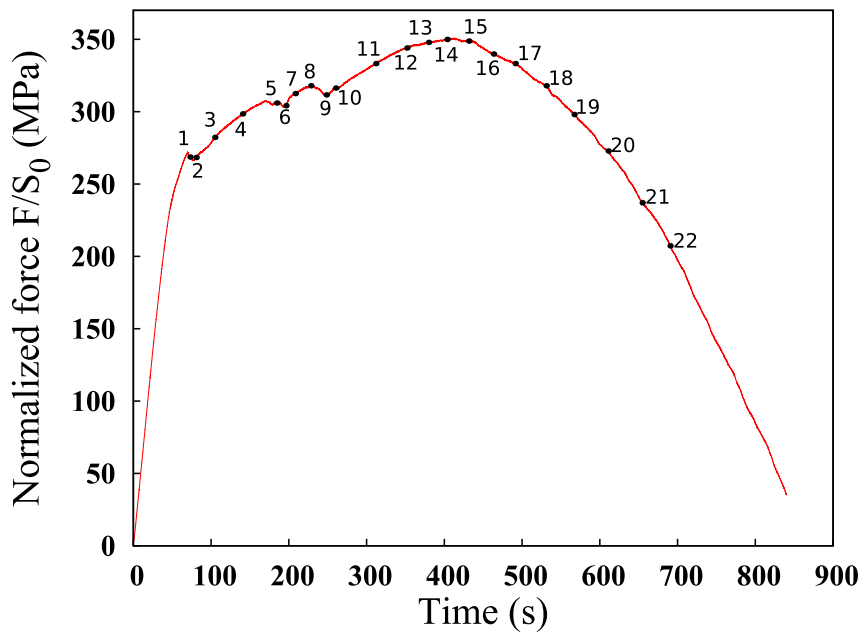
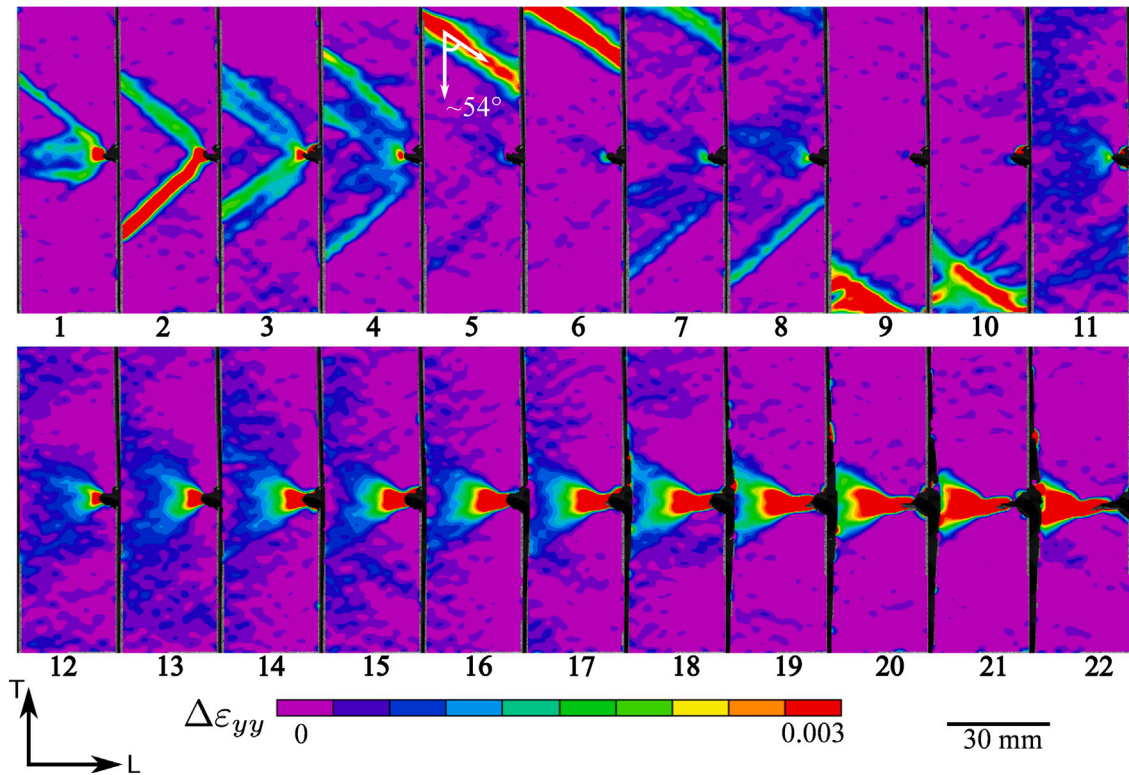


Fig. 3. Load–displacement curve and fracture energy U_i divided into the crack initiation energy U_i and the crack propagation energy U_p .

Calibration was made at room temperature. Using the calibration target, the spatial resolution is $77.6 \mu\text{m}/\text{pixel}$ for these four tests. A subset size of 25×25 pixels is used for correlation. The calculation step size (grid point spacing) is 8 pixels. These settings



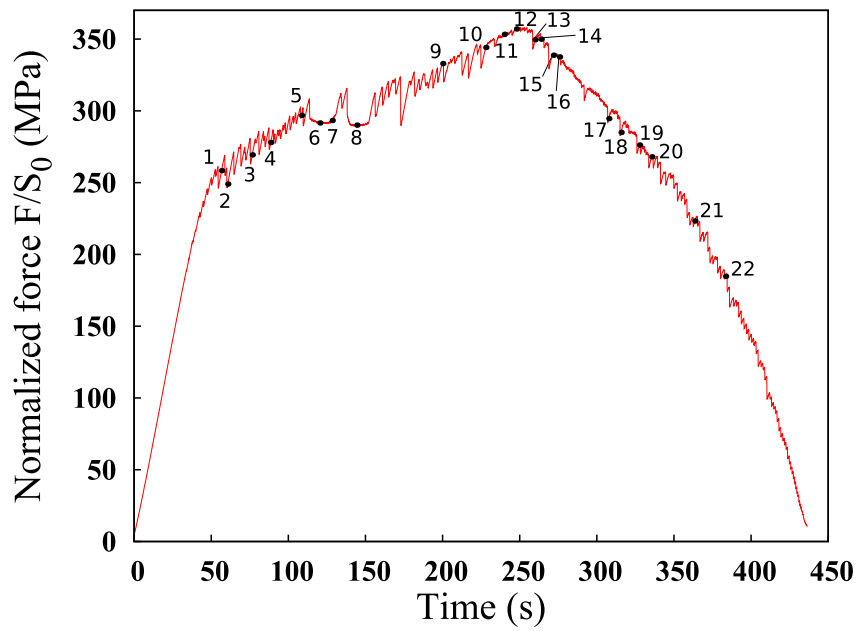
(a)



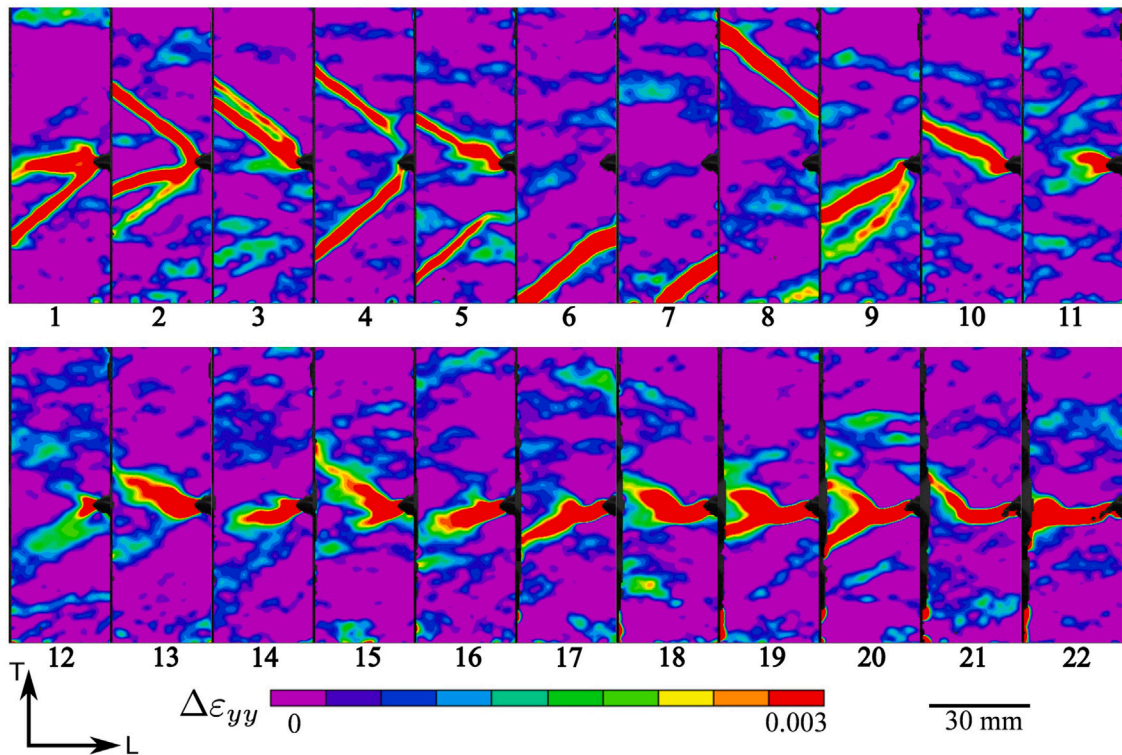
(b)

Fig. 4. Stress-time curve and incremental strain field (maximum scale fixed at 0.003; $\Delta t = 4$ s corresponding to strain rate $7.5 \times 10^{-4} \text{s}^{-1}$) measured by DIC for specimen A at 20°C with loading rate $v = 0.01$ mm/s. The number below each snapshot in (b) corresponds to that on the curve in (a) representing different stages.

are within the optimal range of configurations in VIC-3D (Correlated Solutions). More details about the DIC technique can be found in Sutton (2008). The image acquisition rate during loading was 2.5 fps (one image every 0.4 s) for the two tests with loading rates of



(a)



(b)

Fig. 5. Stress-time curve and incremental strain field (maximum scale fixed at 0.003; $\Delta t = 4$ s corresponding to a strain rate of $7.5 \times 10^{-4} \text{s}^{-1}$) measured by DIC for specimen B at 175 °C with a loading rate of $v = 0.01$ mm/s. The number below each snapshot in (b) corresponds to that on the curve in (a) representing different stages.

0.01 mm/s and 1.0 fps for those with a loading rate of 0.002 mm/s. The heterogeneous strain on the surface of the tested specimens was calculated using VIC-3D (Correlated Solutions). The Green-Lagrange strain measurement was computed from the displacement

field found by correlation. The strain calculation in VIC-3D is similar to the FEM algorithm. The input for the strain calculation is the grid of data points. A local mesh of planar triangles is created by connecting these points. The element size is controlled by the “step size” in the software. The displacement inside a triangular element is obtained by linear approximation (polynomial fit). The obtained displacement gradient is used for computing the Green–Lagrange strain. The term ϵ_{yy} used in the following is the second component of the Green–Lagrange strain tensor. The loading direction y is parallel to the T direction in Fig. 1.

2.4. Localization band morphology

PLC bands form as a consequence of the strain rate softening phenomenon (Graff et al., 2008; Kubin and Estrin, 1984). These bands can be observed by plotting the plastic strain rate variable \dot{p} in the FEM simulations. From the DIC measurement, the total strain is estimated by comparison of the reference and current images. To show the strain rate localization bands, an incremental correlation strategy was performed by correlating two successive images with a constant time interval Δt . The strain rate $\dot{\epsilon}$ can approximately be calculated as $\Delta\epsilon/\Delta t$. Theoretically, the smaller the time interval, the closer the strain rate will be to the instantaneous value. However, the measurement noise could be a problem with small time intervals as the signal-to-noise ratio would be degraded.

The time increment was chosen to be $\Delta t = 4$ s for the two tests with a loading rate of $v = 0.01$ mm/s. To make a direct comparison between the tests at 20 °C and 175 °C, the incremental strain fields ($\Delta\epsilon_{yy}$) corresponding to 22 different stages for each case are displayed in Figs. 4 and 5 respectively. The maximum scale of $\Delta\epsilon_{yy}$ is fixed at 0.003 which indicates a strain rate $\dot{\epsilon}_{yy} = 0.003/4$ s⁻¹ = 0.00075 s⁻¹. With the marked numbers, the corresponding incremental strain pattern could be associated with the force–time curve.

For the test at 20 °C (Fig. 4), the propagation bands were only observed before stage No. 11. There are two force drops at No.6 and 9 on the force–time curve. These two force drops are related to the propagating localization bands reaching the grips. In addition, the angle of the propagating bands to the loading direction is around 54° as indicated in No.5. These propagating localization bands are interpreted as Lüders bands, as expected at room temperature (Marais et al., 2012).

For the test at 175 °C (Fig. 5), the localization bands also initiated around the notch area then propagated to the grip area (see Fig. 5). The two force plateaux (stage No. 6 and 8) on the force–time curve correspond to two propagating localization bands. After stage No. 8 at 175 °C, the localization events were mostly concentrated around the notch flipping up and down. No more propagation bands were observed. In contrast, the plastic zone was very stable at 20 °C after stage No. 11. No significant flipping behaviour could be seen. In addition, the visible cracks at the surface were observed around stage No. 14 at 20 °C and around stage No. 12 at 175 °C.

Another comparative group contains two tests each with a loading rate $v = 0.002$ mm/s. The time increment for correlation is $\Delta t = 20$ s for these two tests. The maximum scale is also chosen to be 0.003 which indicates a strain rate $\dot{\epsilon} = 0.003/20 = 0.00015$ s⁻¹ that is 5 times smaller than the previous tests at a loading rate of $v = 0.01$ mm/s. The incremental strain patterns corresponding to different stages are shown in Figs. 6 and 7.

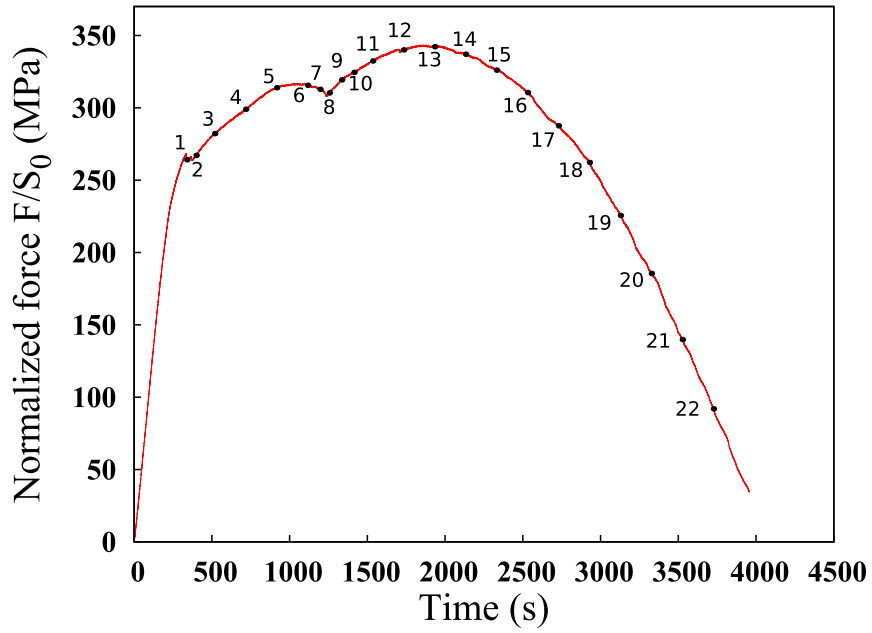
For the test at 20 °C (Fig. 6), the propagative bands were annihilated after stage No. 9 which corresponds to the end of a force drop on the force–time curve. Comparing with the homologous test with a higher loading rate (see Fig. 4), there is only one significant force drop on the curve. This is certainly due to the two propagating bands arriving simultaneously at the grip. Similarly, the plastic zone is very stable during the crack propagation after stage No. 11.

At 175 °C (Fig. 7), even the main propagating bands (from No.8 to No.10) showed more flipping behaviour than in the test at $v = 0.01$ mm/s. These two bands seem to compete with each other by alternating up and down. Similar flipping behaviour of localization bands can also be noticed during crack propagation.

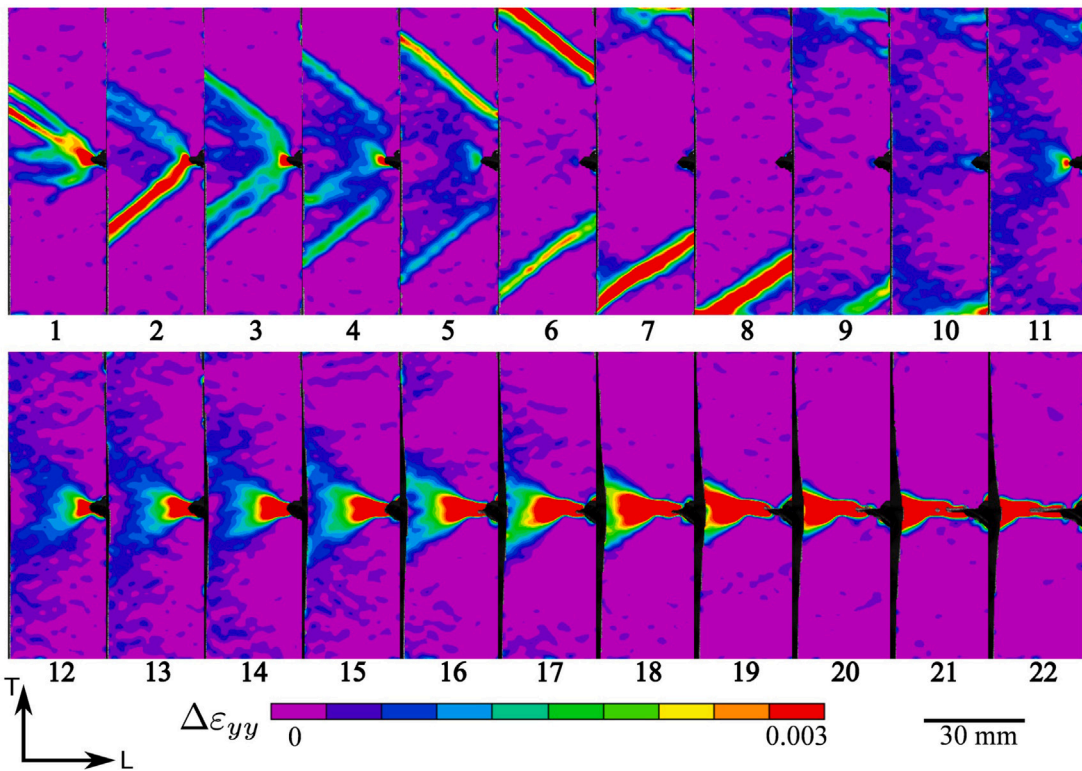
2.5. Spatio-temporal kinematics of localization bands

To better illustrate the evolution of localization bands (Lüders and PLC), so-called spatio-temporal patterns are used for describing the location of bands at different stages of experiments as practised by many authors (Chmelfik et al., 2002; Benallal et al., 2008; Mazière et al., 2010). A line (Y_{mid}) was positioned in the centre of the specimen in order to measure the incremental strain evolution along this line over the whole deformation process (see Fig. 8(a)). The spatio-temporal patterns of these 4 tests are shown in Fig. 8 together with the corresponding force–time curves. The colour contour is a measure of the strain rate $\dot{\epsilon}_{yy} = \Delta\epsilon_{yy}/\Delta t$. It can be seen that the bands propagated with two significantly different velocities. At the beginning, the Lüders bands initiated at the notch tip (see Fig. 4(b) 1–3 or Fig. 5(b) 1–4). Due to the higher concentration of deformation around the notch, the bands propagate to the two grips with one side trapped by the notch area which reduced the propagation velocity. Once escaped from the notch area, the band accelerates. Thus, it is possible to observe two different slopes for the bands in the spatio-temporal patterns. The velocity of the free propagating bands is 3–4 times higher than the bands around the notch. The acceleration of band propagation is also associated with the nearly constant force plateau (No.6–8) on the force–time curve. After the force plateau, the propagating bands disappeared. At 20 °C, no more bands could be observed after the propagation of two Lüders bands. See Section 4.2 for a detailed discussion of the difference between Lüders and PLC bands. At 175 °C, new PLC bands continuously initiate around the notch tip. In addition, at 175 °C, the nucleation of localization bands is always associated with force drops. The flipping behaviour of localization bands during crack propagation at 175 °C, as shown in Figs. 5 and 7, is also confirmed.

To draw a quantitative comparison, the evolution of the maximum strain rate along a line Y_{mid} (see Fig. 8(a)) is presented in Fig. 9. At 20 °C, the first force drop yields strong localization bands around the notch. Then the strain rate inside the bands becomes weaker until reaching the force plateau. During the free propagation phase, the strain rate inside localization bands is higher than

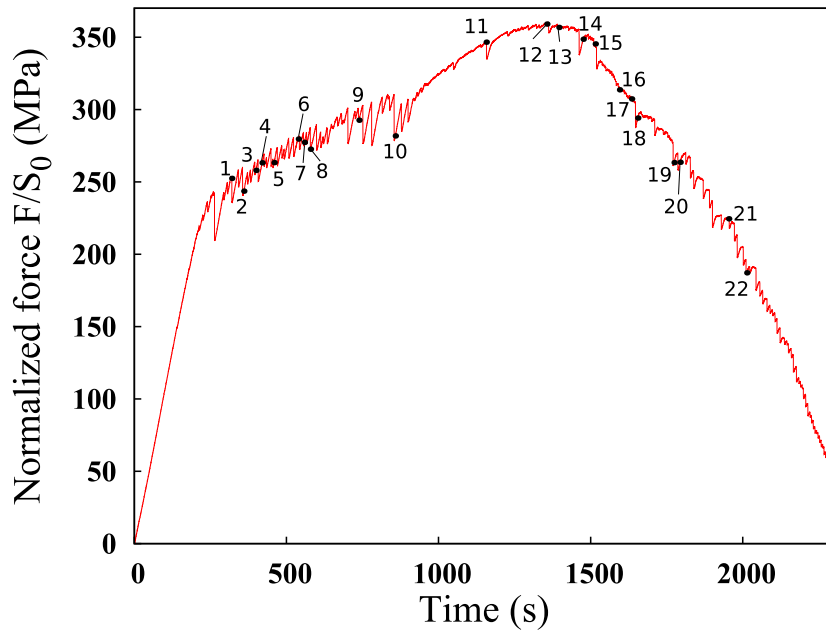


(a)

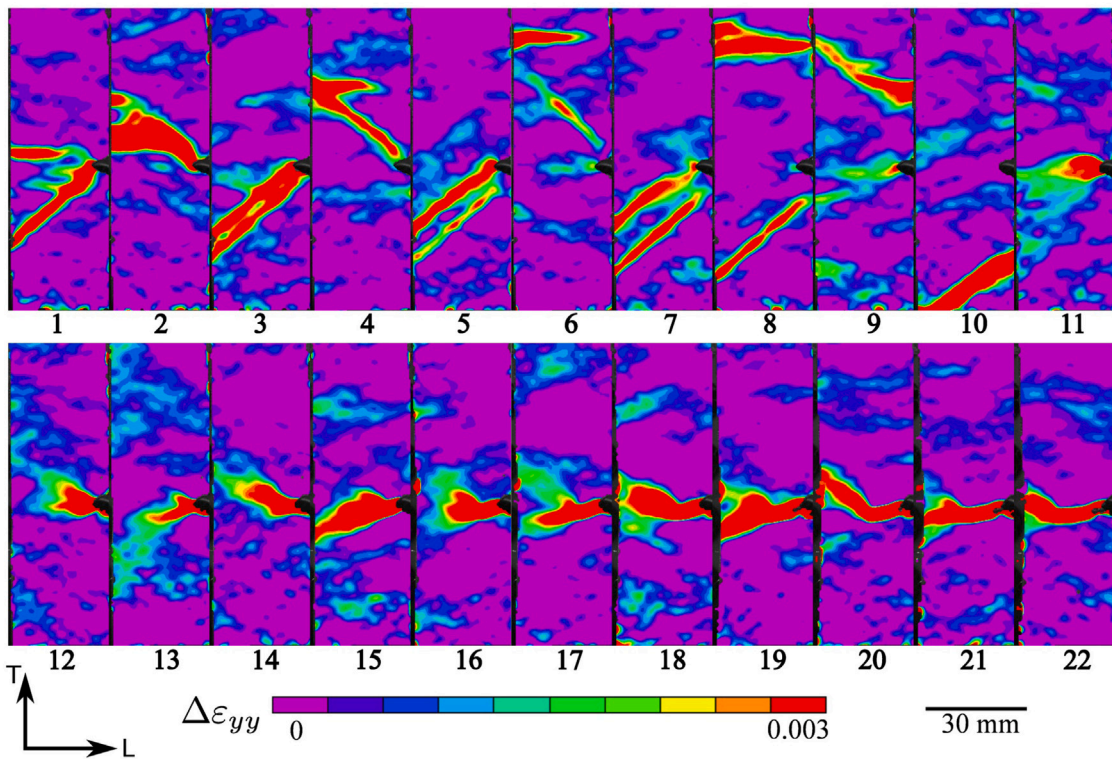


(b)

Fig. 6. Stress-time curve and incremental strain field (maximum scale fixed at 0.003; $\Delta t = 20$ s corresponding to strain rate $1.5 \times 10^{-4} \text{ s}^{-1}$) measured by DIC for specimen C at 20 °C with a loading rate of $v = 0.002 \text{ mm/s}$.



(a)



(b)

Fig. 7. Stress-time curve and incremental strain field (maximum scale fixed at 0.003; $\Delta t = 20$ s corresponding to a strain rate of $1.5 \times 10^{-4} \text{ s}^{-1}$) measured by DIC for specimen D at 175°C with a loading rate of $v = 0.002 \text{ mm/s}$.

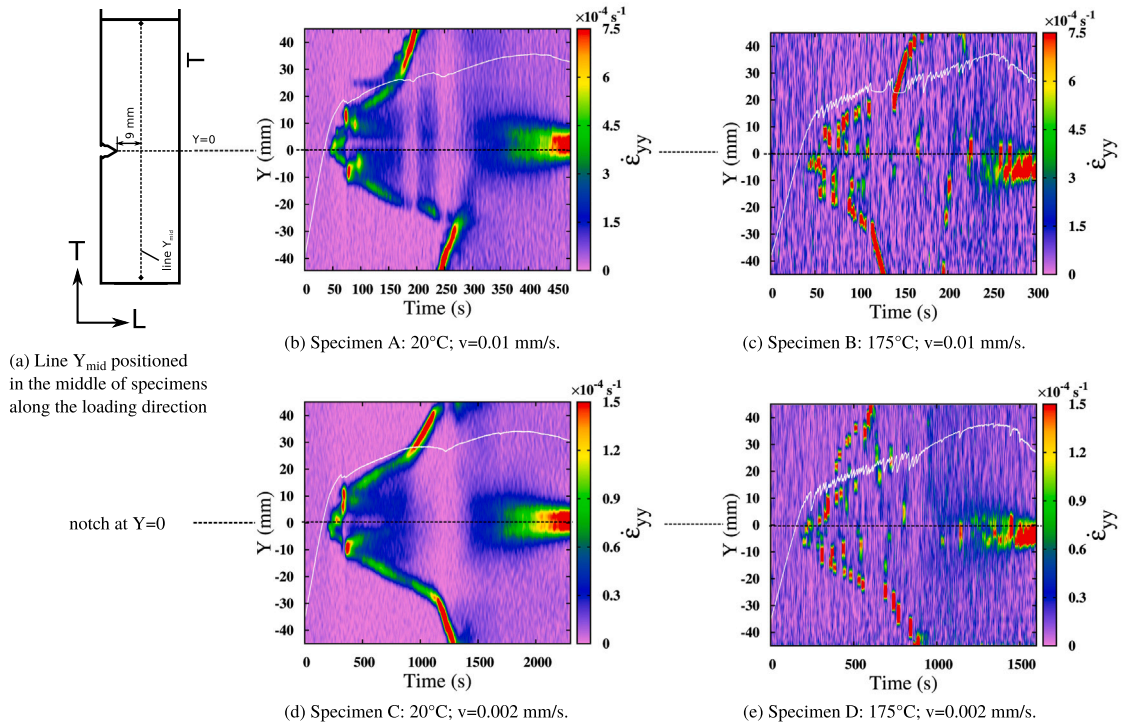


Fig. 8. Spatio-temporal patterns of the four tests measured along line Y_{mid} . The notch position is at $Y = 0$ as shown in (a).

the one in the bands trapped at the notch tip area. At 175 °C, the strain rate inside localization bands did not decrease too much due to the simultaneously occurring PLC effect. The strain rate level inside a band at 175 °C is significantly higher than that at room temperature. The measured maximum strain rate profiles at 175 °C show many peaks due to many intense PLC serrations. A direct comparison of the strain rate in a single band is given below in Section 3.3.

The strain fields in a region of interest (ROI) at the maximum force for specimen A and at the same displacement (= 1.96 mm) for specimen B are presented in Fig. 10(a) and (b). With the same strain scale, the plastic zone of “butterfly” shape during crack initiation at 20 °C is less concentrated than that at 175 °C. The angle between the two “wings” of the plastic zone is smaller at 175 °C than 20 °C. It can also be seen that the plastic deformation at 175 °C is exaggerated by the passage of previous localization bands which left behind a flame-like plastic zone. Fig. 10(c) and (d) also give a measurement of the strain evolution along a line closer to the notch. A similar approach can be found in Zavattieri et al. (2009). The line is perpendicular to the crack propagation direction at 4 mm from the notch tip. The profile of accumulated strain along this line from the initial state until the crack reaches this area (then the correlation fails due to paint cracking). Different evolutions at 175 °C and at 20 °C are observed. At 175 °C, the evolution of strain is less symmetrical. The lower part of the plastic zone (left peak) becomes dominant after reaching $\epsilon_{yy} = 0.061$. At 20 °C, the two peaks keep growing until $\epsilon_{yy} = 0.165$ followed by a more important plastic zone in the central area between the two “wings”. This phenomenon has also been found in the tests with a loading rate of $v = 0.002$ mm/s. A reasonable explanation for the loss of symmetry of plastic zone evolution at 175 °C would be the key for explaining the slant fracture at 175 °C.

The corresponding position on the global force–displacement curve denoting the onset of non symmetric plastic zone is marked in the zoom view of Fig. 10. For 175 °C, this point appears before the visible crack propagation. However, at 20 °C, this point appeared almost at the same time as crack propagation. Considering that the line Y is placed at 4 mm to the notch tip, the loss of symmetry at the actual notch tip occurred even earlier. The visible crack indeed propagated along the dominant lower wing (in the current image) of plastic zone at 175 °C. At 20 °C, the crack propagated following the middle plane of the “butterfly” shape plastic zone. Fig. 11 shows the strain evolution on the crack path at these two different temperatures. It can be noticed that the strain increase at 175 °C displays step-like features which is due to the propagation of localization bands. The localization event happened much earlier at 175 °C.

3. Finite element simulations of SENT tests

3.1. Constitutive equations of the strain ageing model

In the current section, in order to simulate the characteristics of the bands observed via DIC, the constitutive equations proposed by Graff et al. (2008) and Mazière et al. (2010) have been retained. The constitutive model is presented within the finite strain

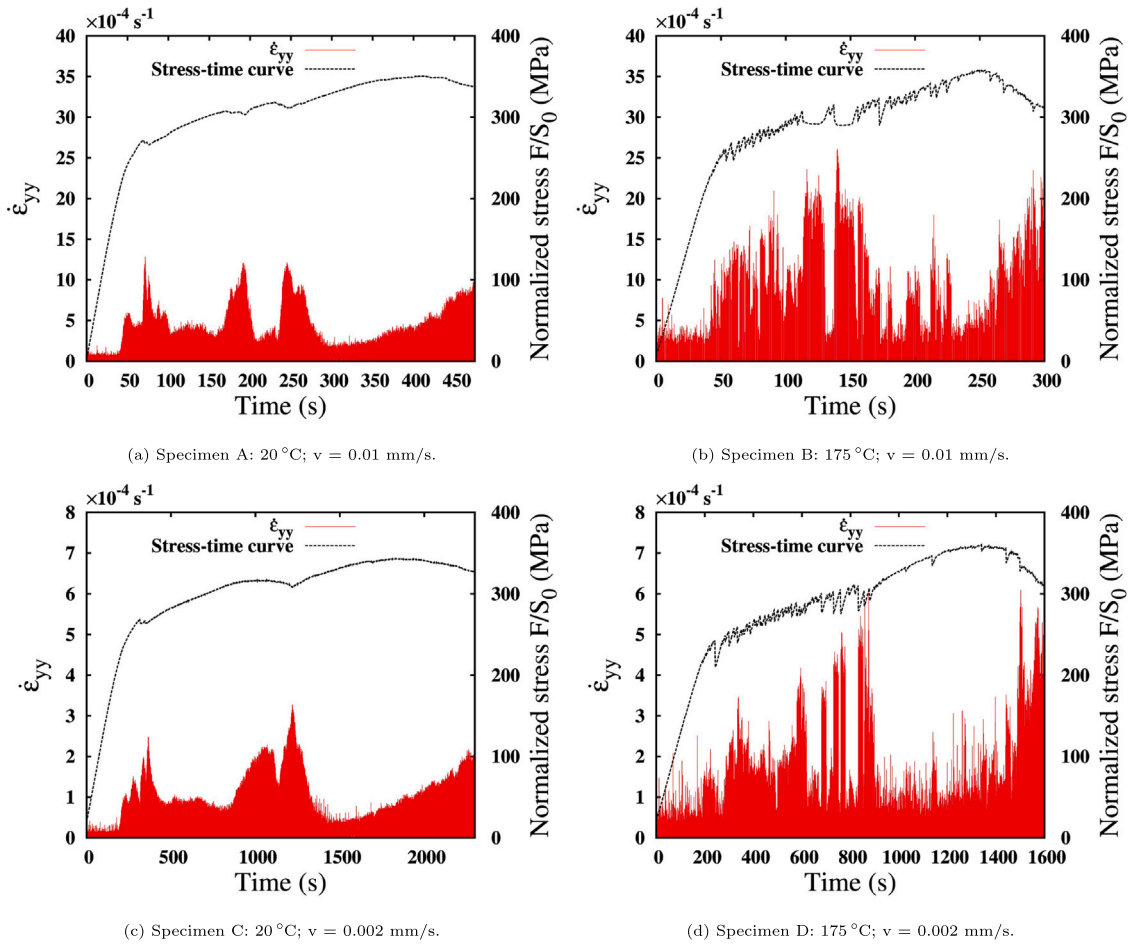


Fig. 9. Maximum strain rate ($\dot{\epsilon}_{yy}$) along the line Y_{mid} in Fig. 8a.

framework using the concept of local objective frames following Besson et al. (2009). The second and fourth order tensors are defined by a single tilde $\tilde{\square}$ and a double tilde $\tilde{\square}$ respectively. Observer invariant stress and strain rate measures $\tilde{\sigma}$ and $\tilde{\dot{\epsilon}}$ are defined by the transformation of the Cauchy stress tensor \tilde{T} and the Eulerian strain rate tensor \tilde{D} into the corotational frame characterized by the rotation $\tilde{Q}(\underline{x},t)$ at each material point:

$$\begin{cases} \tilde{\sigma} = \tilde{Q} \cdot \tilde{T} \cdot \tilde{Q}^T \\ \tilde{\dot{\epsilon}} = \tilde{Q} \cdot \tilde{D} \cdot \tilde{Q}^T \\ \tilde{Q} \text{ such as } \tilde{Q}^T \cdot \dot{\tilde{Q}} = \tilde{\Omega} \text{ (corotational)} \end{cases}$$

where \tilde{D} and $\tilde{\Omega}$ respectively are the symmetric and skew-symmetric parts of the velocity gradient. The strain rate is then decomposed into elastic and plastic parts:

$$\tilde{\dot{\epsilon}} = \tilde{\dot{\epsilon}}^e + \tilde{\dot{\epsilon}}^p, \quad \tilde{\sigma} = \tilde{C} : \tilde{\epsilon}^e \tag{1}$$

where \tilde{C} is the Hooke tensor of elasticity. The plastic flow is described by the normality rule

$$\tilde{\dot{\epsilon}}^p = \dot{p} \tilde{n}, \quad \tilde{n} = \frac{\partial F}{\partial \tilde{\sigma}}, \tag{2}$$

where p is the cumulative plastic strain and the yield function, F , is taken in the form

$$F(\tilde{\sigma}, t_a) = \sigma_{eq}(\tilde{\sigma}) - R(p) - R_a(t_a), \tag{3}$$

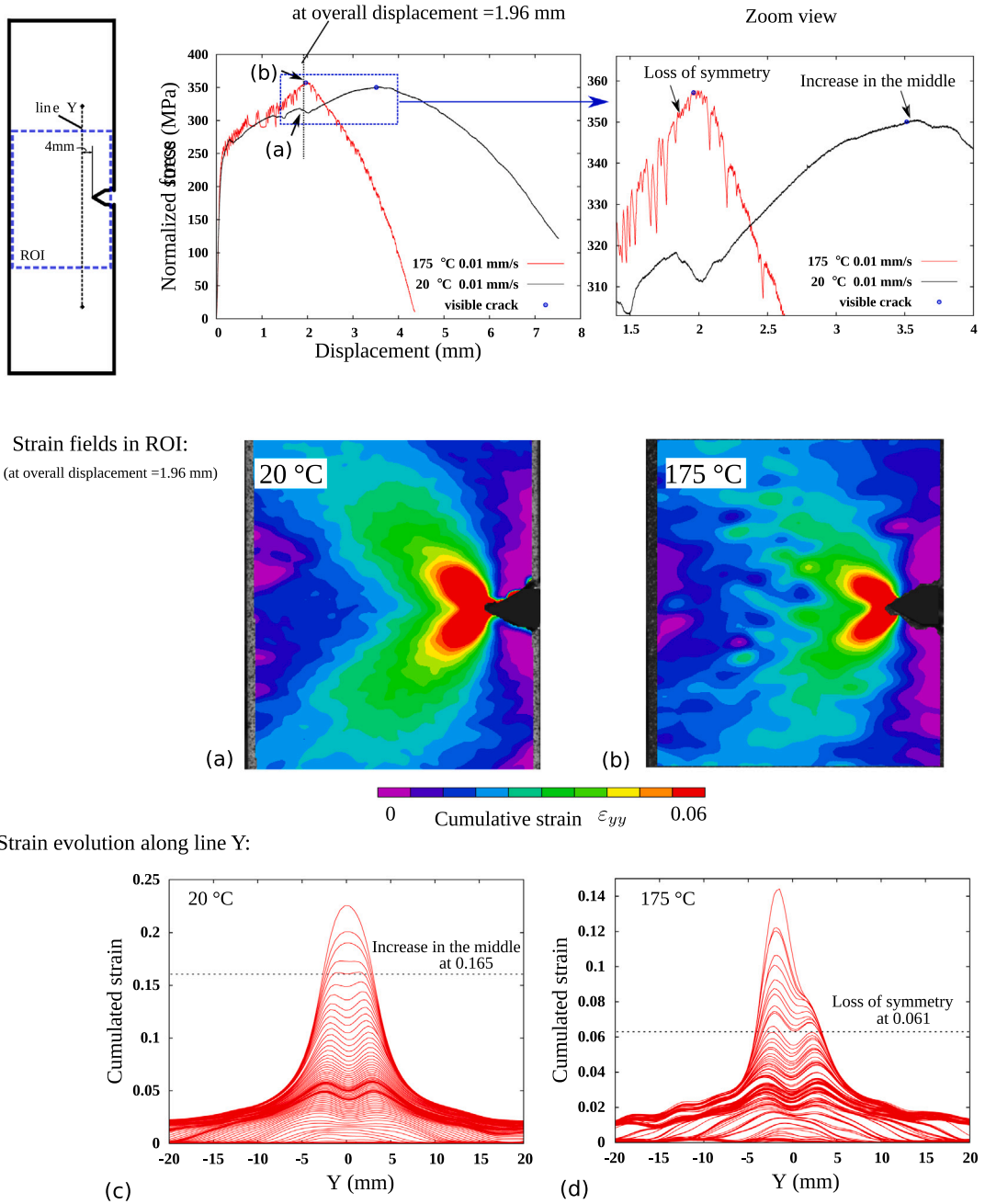


Fig. 10. Comparison of the strain fields in ROI at overall displacement = 1.96 mm for specimen A in subfigure (a) and B in subfigure (b). Comparison of the evolution of cumulated strain along line Y near the notch tip at 20 °C (specimen A) in subfigure (c) and 175 °C (specimen B) in subfigure (d).

where the isotropic hardening term $R(p)$ is

$$R(p) = Hp + Q(1 - e^{-bp}), \tag{4}$$

$$\dot{p} = \dot{\epsilon}_0 \sinh\left(\frac{\max(0, F)}{\sigma_0}\right). \tag{5}$$

The ageing hardening term $R_a(t_a)$ reads

$$R_a(t_a) = P_1 \left[1 - e^{-\left(\frac{t_a}{t_0}\right)^n}\right], \quad t_0(p) = \left(\frac{1}{P_2 p^\alpha}\right)^{1/n}, \quad i_a = 1 - \frac{t_a}{t_0} \dot{p}, \tag{6}$$

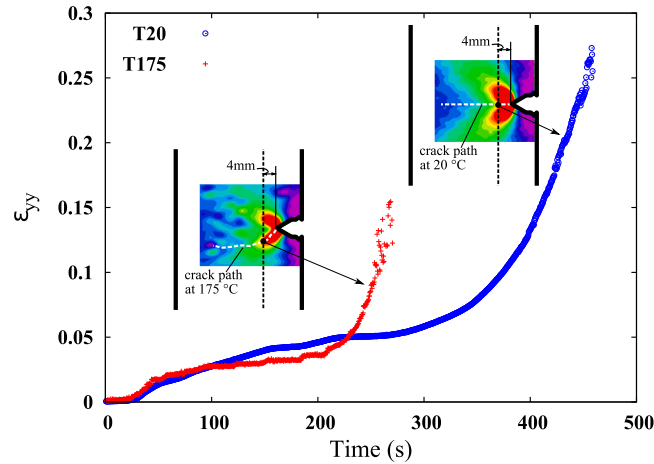


Fig. 11. Strain evolution on the crack path for specimens A and B tested at the same loading rate (0.01 mm/s) and different temperatures.

where P_1 is the maximum stress drop magnitude from a fully pinned state to a fully unpinned state; t_0 characterizes the time of diffusion process; $n = 0.66$ which corresponds to bulk diffusion mechanisms; w characterizes the strain increment associated with unpinning events.

To describe the mechanical response up to fracture, an attempt has been made to couple the current DSA model with damage induced by void growth. The yield function (3) is replaced by the following form (Rousselier, 1987, 2001; Rousselier et al., 2017)

$$F = \frac{\sigma_{eq}}{1-f} + s_1 D_1 f \exp \left[\frac{\sigma_m}{s_1(1-f)} \right] - R(p) - R_a(t_a) \quad (7)$$

where f is the void fraction. In the current section, only the void growth f_g has been considered so that $f = f_g$. Rousselier's model gives a void growth rate almost identical to Rice and Tracey's formula (Rousselier and Quilici, 2015):

$$\dot{f} = \dot{f}_g = \dot{p}(1-f)D_1 f \exp \left(\frac{\sigma_m}{s_1(1-f)} \right). \quad (8)$$

D_1 is a material independent constant, fixed here at $D_1 = 2$ here. Parameter s_1 is chosen to be 275 MPa ($\frac{2}{3}R_m$), and represents the resistance of the metal matrix to void damage. The initial void volume fraction is chosen as 0.001.

3.2. Identification of material parameters

The identification procedure is based on tensile tests. Fig. 12(a) shows the specimen geometry and the spatio-temporal patterns measured by DIC.

The parameters related to the ageing term R_a , such as P_1 , P_2 , n , w , α were based on the values given in Wang (2011) since the TU48C steel studied by Wang (2011) which is very similar to the current A42 steel. The other hardening parameters at 175 °C are also taken from the function proposed by Wang (2011). The hardening parameters at 20 °C are identified from the experimental tensile curves of our material (A42). An optimization procedure using the Levenberg–Marquardt algorithm is used to minimize the deviation between data from material point simulations and those of the smoothed experimental stress–strain curves of tensile tests. This strategy avoids time-consuming FEM simulations on full dimension specimens. The complete constitutive model parameters used for the current section are presented in Table 3.

Fig. 12(b) shows the uni-axial tensile curve at room temperature with applied strain rate 10^{-2} s^{-1} and 10^{-3} s^{-1} . At this temperature, there is no PLC effect. The tensile curves do not exhibit a negative strain-rate sensitivity. The Lüders yield peak and plateau can be observed. The simulation result at 10^{-2} s^{-1} on a 2D mesh is also plotted in Fig. 12(b). The simulated curve is in good agreement (<6%) with the experimental one. Fig. 12(c) gives the experimental tensile curve at 175 °C and 10^{-3} s^{-1} . The simulated curve for the same condition is added for comparison. It can be noted that the material at 175 °C exhibits both Lüders and PLC phenomena.

3.3. 3D FEM simulations with strain ageing model

Fig. 13 shows the 3D mesh used in the current section, which contains 6184 elements (C3D20R element with quadratic interpolation and a reduced number of integration points) and 29 499 nodes in total. A piece of the upper half specimen is shown. In the refined area, there are 8 elements ($0.625 \times 0.625 \times 0.625 \text{ mm}^3$) through the thickness. Outside this region, coarse meshes are used to save computation time. The evolution of the calculated stress triaxiality at mid-thickness of the notch tip area of the current SENT specimen is also shown in Fig. 13.

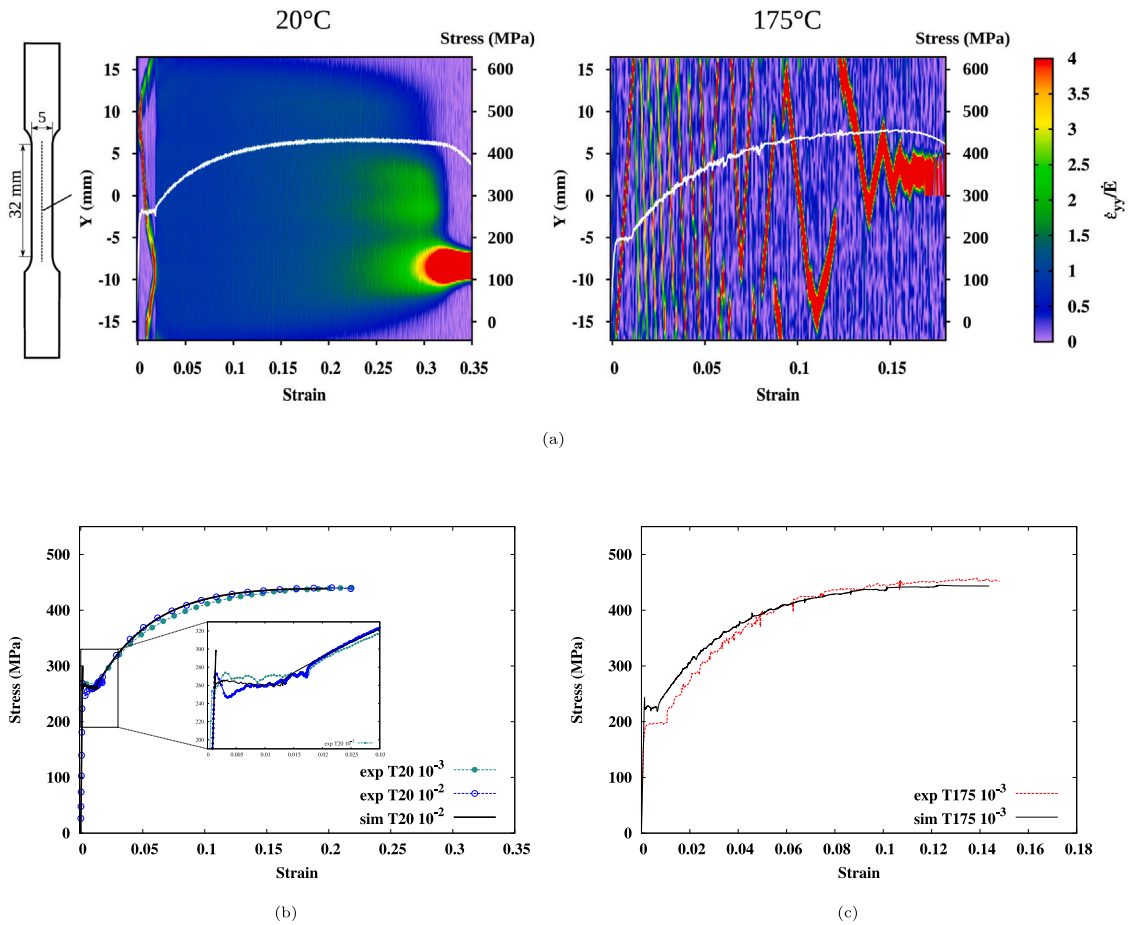


Fig. 12. (a) Tensile specimen and the spatio-temporal patterns at 20 °C and 175 °C at a strain rate $\dot{E} = 10^{-3} \text{ s}^{-1}$. (b) Experimental and simulated stress–strain curves of the tensile test carried out at room temperature for two strain rates. (c) experimental and simulated tensile curves at 175 °C and strain rate 10^{-3} s^{-1} .

Table 3
Parameters used at 20 °C and 175 °C for C–Mn steel A42.

20 °C						
E (GPa)	ν	P_1 (MPa)	n	w	$P_2(\text{s}^{-n})$	α
210	0.3	94	0.66	2×10^{-4}	0.01	0.26
R_0 (MPa)	Q (MPa)	b	H (MPa)	$\dot{\epsilon}_0$ (s $^{-1}$)	σ_0 (MPa)	t_{a0} (s)
200	256	20	360	9.16×10^{-4}	4.11	5×10^6
175 °C						
E (GPa)	ν	P_1 (MPa)	n	w	$P_2(\text{s}^{-n})$	α
199.83	0.3	84.84	0.66	2×10^{-4}	0.46	0.19
R_0 (MPa)	Q (MPa)	b	H (MPa)	$\dot{\epsilon}_0$ (s $^{-1}$)	σ_0 (MPa)	t_{a0} (s)
178.86	273.5	29.6	360	9.45×10^{-4}	4.50	10^4

As the tests at a loading rate of 0.002 mm/s generally showed similar results with those at 0.01 mm/s, only the comparison between experimental and numerical results with loading rate 0.01 mm/s is presented here. Fig. 14(a) presents the 3D simulation curves of SENT specimen at 20 °C with a loading rate of $v = 0.01 \text{ mm/s}$. The experimental curves are superimposed with numerical ones. It can be seen that the initial yield peak is overestimated by the FEM simulation. The stress drop reproduced by the simulation occurs earlier than in the experiment. The simulated hardening before fracture is consistent with the experimental curve. Without the damage mechanism, the current constitutive model is not able to describe the descending part of the global stress–displacement curve. Void damage occurs at a very early stage at the notch tip. Therefore, the stress–displacement curves produced by the strain ageing model coupled with damage are also presented in Fig. 14. The prediction has been improved significantly at 20 °C. The 3D

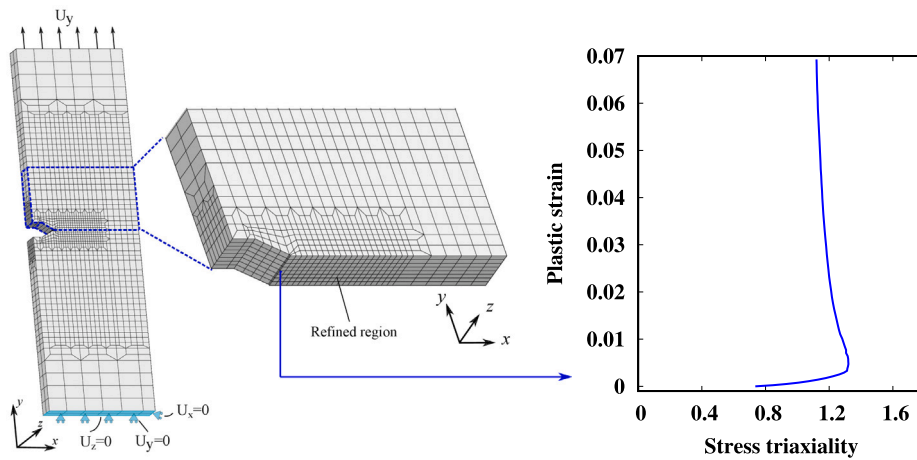


Fig. 13. 3D mesh with refined area around the notch and stress triaxiality calculated at notch tip.

simulation results of the test at 175 °C with $v = 0.01$ mm/s are presented in Fig. 14(b). The huge ductility loss at 175 °C is not well predicted with the same damage parameters.

3.4. Spatio-temporal patterns and localization bands from FE simulations

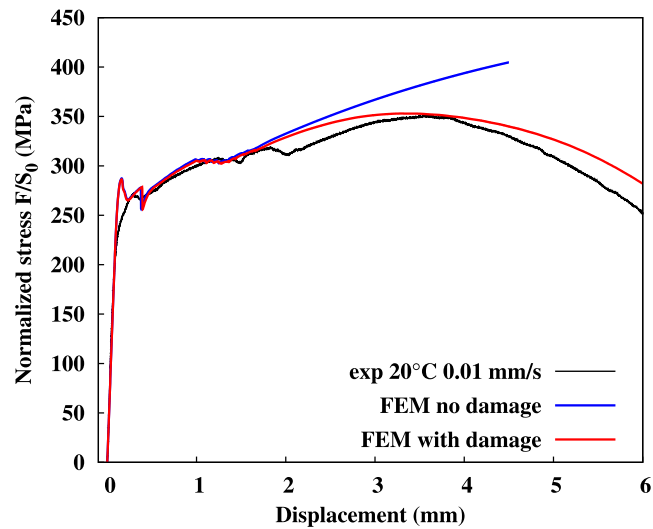
The spatio-temporal patterns of FE simulations with a loading rate of $v = 0.01$ mm/s are plotted in Fig. 15. These simulations are carried out only with the strain ageing model without damage. There are considerable similarities between these numerical patterns and those measured by DIC (see Fig. 8). The evolution of localization bands produced by FE simulation at 20 °C is almost identical to the experiment. The effect of notch area for slowing down band propagation is correctly predicted. Two different velocity slopes can be seen in the spatio-temporal patterns for both temperatures. In addition, the two propagating localization bands propagate symmetrically and arrive at the two grips at the same time which is not always the case in the experiments. At 175 °C, the flipping behaviour of localization bands during propagation is also properly reproduced by the model. However, the localization bands around the notch (after the annihilation of propagating bands) show more propagative behaviour in the simulation. In the experiment, these bands are more intermittent without propagation. Fig. 15(d) gives the band velocities measured from the spatio-temporal patterns of DIC and simulations. The velocities of two types of propagating bands at 175 °C are in good agreement with DIC measurement. The velocity of free propagating bands at 20 °C is slightly underestimated.

Fig. 16 shows the band morphology produced by FE simulations with a loading rate of $v = 0.01$ mm/s. At 20 °C, only two propagating bands are obtained. These two bands propagate to both ends of the specimen simultaneously. As indicated at $t = 117$ s, the angle of the propagating band is 51.25° which is very close to the DIC measurement presented in Fig. 4. The plastic zone around the notch is very stable after the annihilation of these initial bands. At 175 °C, the band shape as well as the alternating behaviour are captured correctly. Although the strain rate localization bands in the thickness plane cannot be observed directly by DIC measurement, the current numerical simulations enable sufficient information to be obtained in the thickness direction. The strain rate localization behaviour in the thickness plane is shown in Fig. 16(a) and (b) at each time stage of the corresponding front view. Multiple slant strain rate localization bands can be observed frequently for the simulation at 175 °C. In contrast, no slant bands were found for simulation at room temperature except for the very early band nucleation stage. The slanted localization bands might be the precursor of a slant fracture as mentioned in Table 2. This issue will be discussed in Section 4.3.

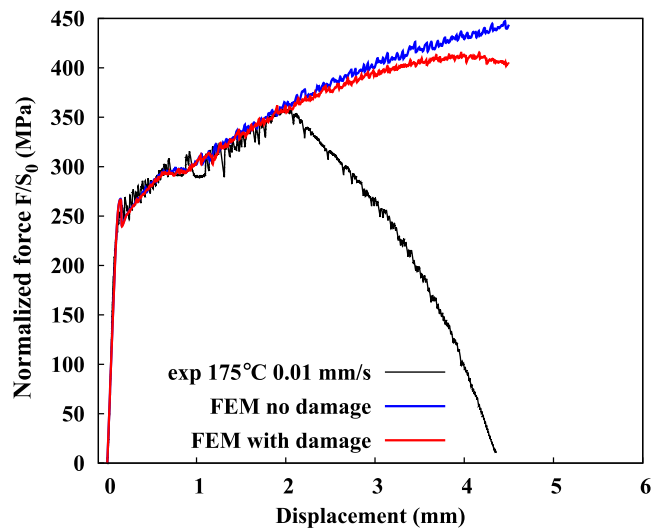
To compare with Figs. 9, 17 shows the evolution of maximum strain rate along the line Y_{mid} produced by FE simulations. The strain rate in the band of first stress drop is higher than the following bands which is consistent with DIC measurement. However, the amplitude is overestimated compared with experiments. When the bands start to propagate without the influence of the notch tip area, associated with a stress plateau, the strain rate in bands attains again a peak level. The strain rate in bands at 175 °C is higher than at 20 °C. At 175 °C the maximum strain rate did not decrease to a lower level after the first stress drop, which is due to the continuously propagating PLC bands.

4. Discussion

The kinematics and mechanical properties of localization bands due to strain ageing were studied by DIC and finite element simulations in this work. The DIC measurements revealed, for the first time, the kinematics of PLC bands around the notch tip of C–Mn steel SENT specimen at high temperature. The room temperature experiments also demonstrated the characteristics of Lüders effect that differ from ordinary smooth tensile specimens. In this discussion, the DIC and simulation results obtained in the previous sections are compared with those in the literature.



(a) FE simulation results of specimen A.



(b) FE simulation results of specimen B.

Fig. 14. Stress–displacement curves of FE simulation for the two tests at a loading rate of 0.01 mm/s.

4.1. The global stress–displacement curve

The Lüders effect in tensile tests is characterized by an upper yield stress at elastic–plastic transition point followed by a stress plateau with lower constant stress level. In the current SENT tests, a stress drop can still be observed at 20 °C, but it occurred later than the elastic–plastic transition point (see Fig. 4). Unlike the tensile test, the yield stress of the SENT specimen increases during the yield stage. This phenomenon is related to the notch tip effect. The area around the notch undergoes severe plastic deformation. The Lüders bands initiate in this region earlier than the rest of specimen which results in a nonlinearity on the global stress–displacement curve without visible stress drop. In the less deformed area, the initially pinned dislocations are not able to break away from the Cottrell atmosphere which results in an increase of global stress. When the front of Lüders band reaches the whole width of the specimen, a stress drop becomes visible on the global stress curve. Appendix gives a comparison between the simulation results without Lüders effect and those involving the Lüders effect. The range of Lüders effect on the global curve can be verified by these simulations. In addition, to avoid measurement uncertainty, the possible effect of out of plane displacement during the experiments is also demonstrated on the global curve by simulations (see Appendix). This notch effect on the global stress due to Lüders effect has also been observed by Han et al. (2011) in Q345 steel at room temperature. The DIC measurement presented in the current work confirms the assumption about the Lüders band initiation around a notch tip discussed by Han et al.

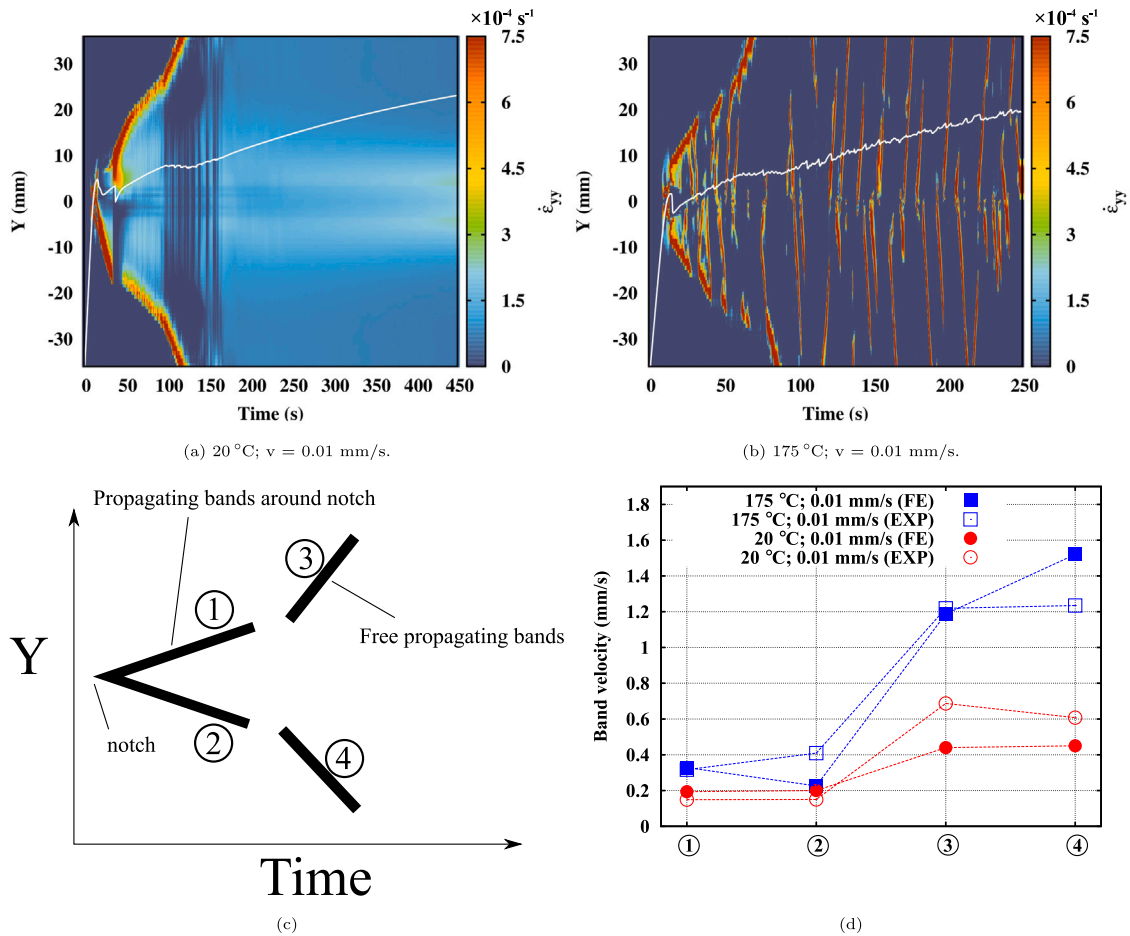


Fig. 15. Spatio-temporal patterns obtained from FE simulations to be compared with the experimental results in Fig. 8(a) and (b). (c) Schematic representations of the band evolution in a spatio-temporal pattern and the comparison of velocities of Lüders band propagation measured by DIC and simulations at $v = 0.01 \text{ mm/s}$ (d).

(2011). In the work of Han et al. (2011), due to a lack of DIC measurement, the author did not provide any information about the spatio-temporal evolution of Lüders bands.

At 175 °C, it is more difficult to identify the Lüders stress drop due to the superposition of PLC serrations. At this temperature, the serrations started right after the elastic–plastic transition point. The PLC serrations did not change the shape of global stress curve.

The huge drop of ductility and toughness at 175 °C is observed for both tested loading rates (0.01 mm/s and 0.002 mm/s) which proved the reproducibility of this result. The factor around 2 of toughness drop at 175 °C is consistent with the results reported by Wang et al. (2012). The simulations using the DSA model only work well for describing the hardening before fracture. The descending part of simulated curves is not in agreement with experiments which is due to the lack of a proper damage mechanism. With the addition of void growth, better results are obtained to describe the descending part of experimental curves at 20 °C. Actually, the damage mechanism starts to influence the global curve before attaining the maximum force. The pre-matured fracture at 175 °C is not reproduced using the same damage parameters for both temperatures. This is a limitation of the damage model which will require future work. More sophisticated damage modelling combining the Rousselier damage model, polycrystalline plasticity and a Coulomb criterion has been applied recently to model slant fracture in CT specimens by Rousselier et al. (2017).

4.2. Strain field

In smooth tensile specimens, Lüders bands initiate at the edge of the curved transition zone with the grip section of the specimen and propagate through the gauge length of the sample. Three types of bands have been commonly distinguished in simple tension under constant applied strain rate and temperature such as the continuously propagating type A bands, intermittent type B bands and randomly nucleated type C bands (Ait-Amokhtar et al., 2008). The influence of stress concentration areas on the band behaviour was less reported compared to tensile tests.

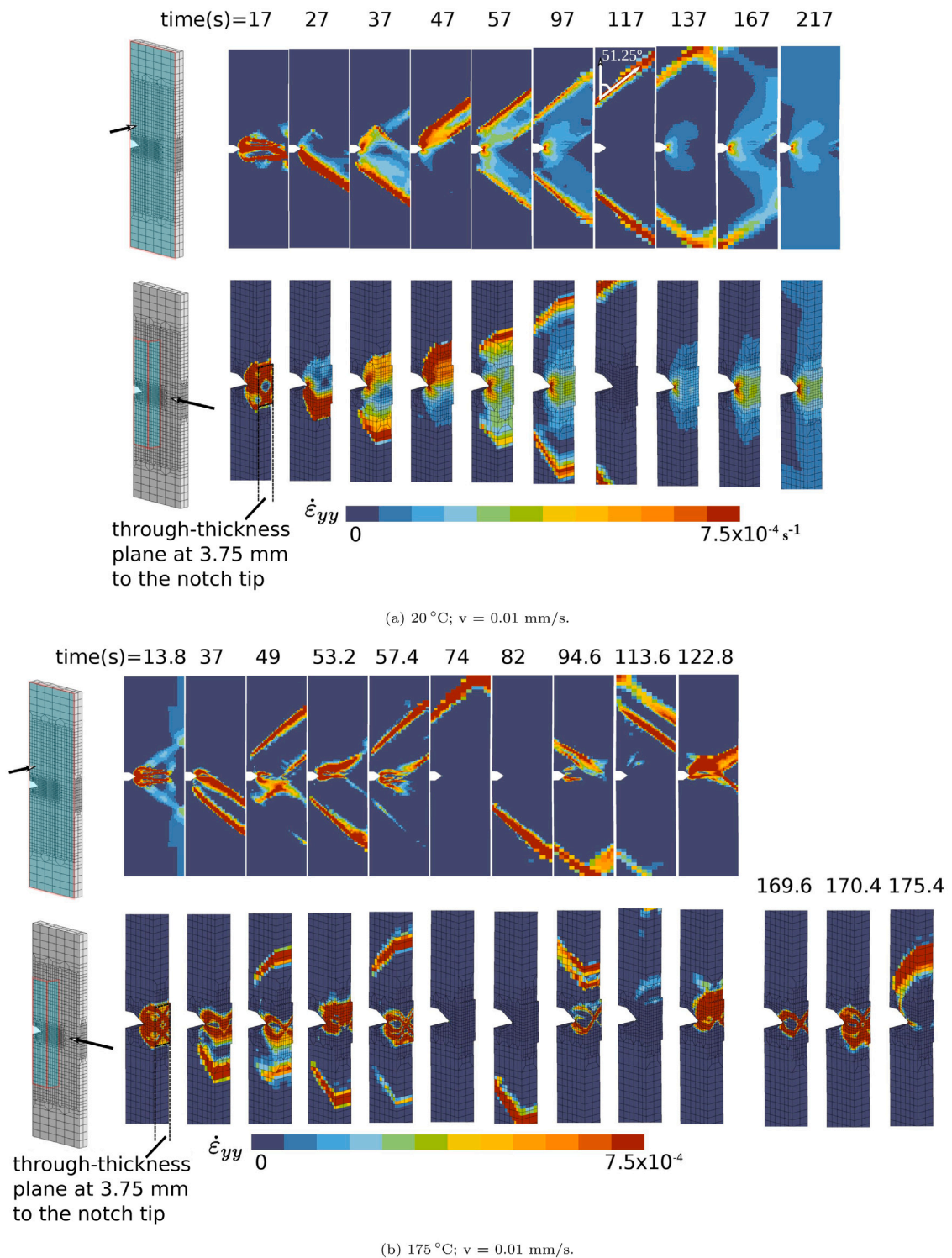


Fig. 16. Localization bands predicted by FE simulations with loading rate $v = 0.01 \text{ mm/s}$ on the surface and in the through thickness plane for (a) room temperature and (b) 175 °C.

The Lüders band morphology in double notched tensile specimens was studied by Graff et al. (2004), Beardsmore et al. (2013) and Xiao et al. (2016). In this specimen type, Lüders bands initiate from the ends of specimens for small notches as in tensile tests.

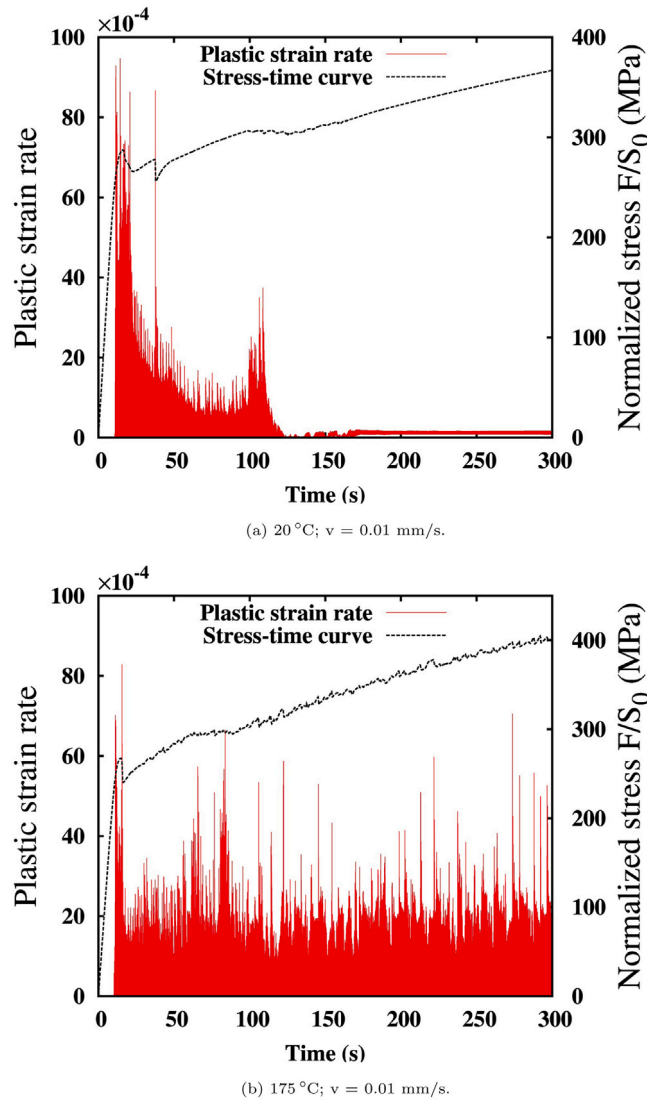


Fig. 17. Maximum strain rate evolution along the centre line Y. To compare with DIC results in Fig. 9(a) and (b).

For large notches, Lüders bands initiate from the notch tip. These bands propagate throughout the whole length of the specimen. The Lüders band morphology in compact tension (CT) specimen has been studied by [Wenman and Chard-Tuckey \(2010\)](#) with DIC measurement and 3D finite element simulations. The Lüders bands in CT specimen are confined to the notch area.

The PLC band features in double notch tensile specimens have been investigated by [Nogueira De Codes and Benallal \(2011\)](#) using digital infrared thermography and DIC. Bands were observed to be trapped in the vicinity of the minimal cross section for double notched specimen. As the tested material did not show any Lüders effect, no more information could be given regarding Lüders band propagation. In contrast, simulations showed that PLC bands could occasionally escape from the minimum section area in double notched specimen ([Benallal et al., 2008](#)). The PLC band morphology in CT specimens was predicted by [Belotteau et al. \(2009\)](#) with the McCormick type DSA model with 2D mesh, and by [Rousselier et al. \(2017\)](#) with 3D mesh, though an experimental validation is still lacking. For a single crack tensile specimen, the PLC bands are found to remain within the notch area as Lüders bands ([Nogueira De Codes and Benallal, 2011](#)).

In the SENT specimen studied in this work, the band kinematics displays different features. We clarified the behaviour of simultaneously occurring Lüders and PLC effects. With DIC measurement, the different scenarios of band propagation at two temperatures can be summarized as:

- 20 °C: Lüders band initiation around notch tip → Continuous band propagation with one side trapped in the notch area → Accelerated continuous free propagation → No PLC bands.

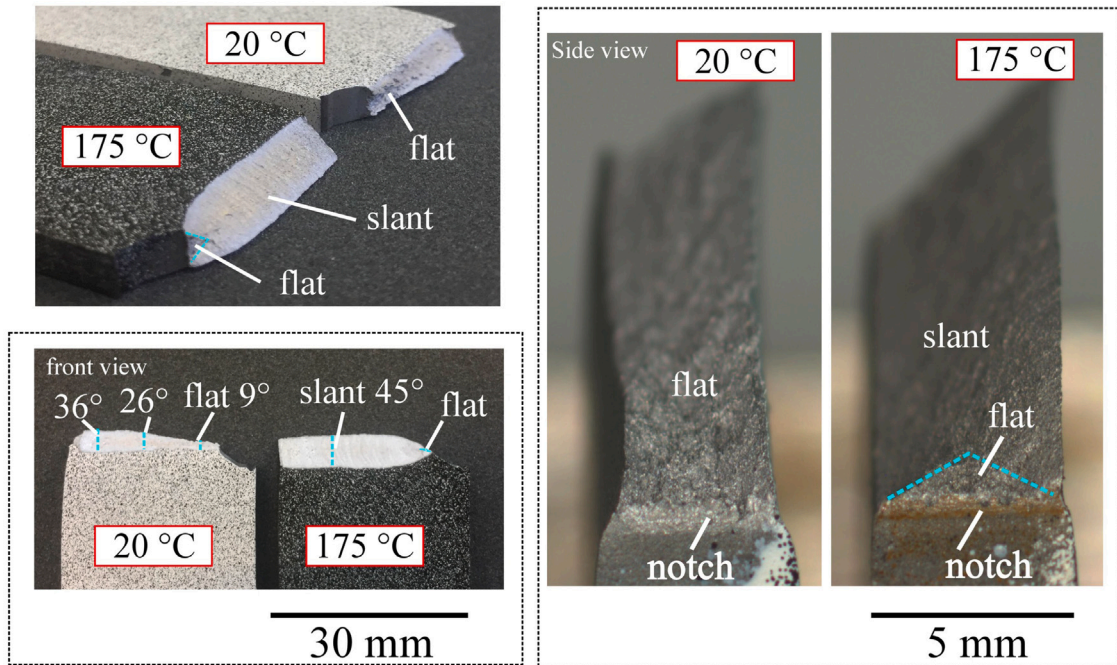


Fig. 18. Fracture surfaces of specimens tested at 175 °C and 20 °C for loading rate 0.01 mm/s. A typical slant fracture with a triangular flat transition zone is observed at 175 °C, while flat fracture is found at 20 °C. The same fracture surfaces are found for the loading rate 0.002 mm/s at corresponding temperatures which are not shown here.

- 175 °C: Lüders and PLC band initiation around notch tip → Intermittent band propagation with one side trapped in the notch area → Accelerated intermittent free propagation → PLC bands flip-flopped around the notch.

Unlike CT specimens (see [Wenman and Chard-Tuckey, 2010](#)), the Lüders bands can propagate throughout the whole length of the specimen in SENT specimens. They propagate only once and were observed at both 20 °C and 175 °C. This effect is caused by the unpinning of initially arrested dislocations which will not be pinned again in the absence of dynamic strain ageing. In contrast, the PLC bands only occur in the notch area at 175 °C. These PLC bands repeatedly occur because of the dynamic strain ageing mechanism. We can confirm these observations from DIC in [Figs. 4–8](#) and by simulations in [Fig. 15](#).

The stress concentrator has a strong influence on the Lüders band propagation (see [Fig. 8](#)). It slows down the propagation velocity for these bands with one side trapped in the notch area. The numerical results capture the notch effect on band propagation as shown in [Fig. 15](#). The velocities at two stages of band propagation are reproduced by numerical simulations, in good agreement with DIC measurement.

The strain rate in propagating bands is higher than that in the bands with one side trapped in the notch area. This could explain the stress plateau at the end of the Lüders effect. When the bands propagate with one side in the notch area, the deformation is still concentrated in the notch tip area. The dislocations in the less deformed area are not fully unpinned which results in an increasing global stress. When the bands started to propagate without the influence of the notch tip, deformation is concentrated in the moving band front which results in a stress plateau.

The flip-flop behaviour of PLC band around the notch tip observed in the current work is to some extent in agreement with that reported in double U-notched specimen by [Nogueira De Codes and Benallal \(2011\)](#). However, the influence of the PLC effect on the Lüders band which results in an intermittent propagation has not been observed before. These scenarios are reproduced successfully with finite element simulations, though the simulated PLC bands showed more propagative feature rather than intermittency.

4.3. Flat and slant fracture mode and fracture mechanisms

As shown in [Fig. 18](#), another interesting finding in the current work is that two different modes of fracture are observed at 20 °C and 175 °C. At 20 °C, the crack remains flat, i.e. normal to the loading direction, until very late stages. In contrast, at 175 °C, a flat to slant transition is observed. This remarkable feature has also been observed in round tensile bars made of TU48C by [Wang et al. \(2011\)](#). The reduction of section thickness, i.e. necking, is significant at 20 °C. The slant fracture is certainly related to the early loss of symmetry in the plastic zone (see [Fig. 10\(d\)](#)). More importantly, in the simulations shown in [Fig. 16](#), slant strain rate bands through the sample thickness are predicted when PLC is active. No such bands are found for simulations at room temperature. The slant bands at elevated temperature may be precursor of the slant fracture and one slant shear band through the thickness plane

may be enhanced by PLC bands. Then the damage would develop in this slanted localization band and result in a slant crack. A similar damage mechanism due to early localization has been reported by [Morgeneyer et al. \(2014\)](#) in thin sheet CT specimen using laminography combined with digital volume correlation. The flip-flop fracture reported by [Simonsen and Törnqvist \(2004\)](#) could also be related to the PLC effect considering that the 5083 aluminium alloy is known to be sensitive to the PLC effect.

To analyse further the local damage mechanisms, fractography is presented in [Appendix A.5](#). Similar micrometre sized dimples can be seen for flat fracture at room temperature and for slant fracture at elevated temperature. The damage mechanism seems classically ductile in both cases. This is why a porous plasticity model is used in the current work in conjunction with the McCormick-type model. Only the flat failure at room temperature can be reproduced achieving fracture energies close to the experiments. However, the absorbed energy at elevated temperature is overpredicted which indicates that a modelling ingredient is still missing in our model for this condition.

In the work by the current authors [Rousselier et al. \(2017\)](#), slant fracture was achieved thanks to the Coulomb fracture criterion applied on the slip system scale. This was motivated by shear fracture features on the fracture surface seen by fractography for the studied aluminium alloy. These features were not found for the C–Mn steel which does not comply therefore with the use this model. In addition, it is likely that slant fracture would also be predicted for the room temperature simulation if the Coulomb fracture model was used at the slip system scale for both temperatures. In other words, the open challenge is not only to reproduce slant fracture alone (It was done before, see e.g. [Morgeneyer et al., 2016](#); [Rousselier et al., 2017](#)), but to reproduce all of its characteristics: flat fracture at room temperature, slant fracture at elevated temperature in addition to the right fracture energies, localization kinetics and micromechanical damage features found by fractography. The present work provides the first steps in this direction by demonstrating the complex and asymmetric plastic strain rate patterns and trends towards slant localization of plasticity.

5. Conclusions

In this work, the impact of the Portevin–Le Chatelier effect on plasticity and fracture ahead of a severe notch is investigated by DIC field measurements at elevated temperature and captured numerically using McCormick type 3D FE simulations. SENT specimens made of C–Mn steel are tested at room temperature and at elevated temperature (175 °C). The main results are summarized below:

(1) The Lüders effect is observed for all the test conditions but in the PLC domain the Lüders bands are perturbed and show intermittent activity. In addition, the deformation rate inside a Lüders band at 175 °C (with PLC) is much higher than its counterpart at 20 °C (without PLC) due to the superposition of the PLC effect. The passage of the first Lüders bands at high temperature is followed by a firework display of PLC bands described quantitatively by the proposed model.

(2) The cumulative plastic zone at 175 °C exhibits loss of symmetry much earlier than at 20 °C. A slant crack is developed following one side of the plastic zone at 175 °C. At 20 °C, as the plastic zone always develops in the middle plane, a flat crack is observed. The non-symmetrical development of the plastic zone at 175 °C shown in [Fig. 10](#) is preceding slant fracture which consequently leads to a reduction of fracture resistance by a factor of two. Slant strain localization bands through the sample thickness are found in simulations in the PLC domain but not at room temperature which might be precursors of the slant fracture in the PLC domain.

(3) The DIC measurements at high temperature show that, due to the presence of PLC effect, the strain localization bands' activity is intermittent. This intermittency and the magnitude of strain carried by the bands are captured by the McCormick-type model presented, thereby validating quantitatively the model in these conditions. The PLC bands during crack propagation are stuck in the crack tip area flipping up and down along loading direction which is also reproduced in the simulation.

(4) Based on fractography observations showing dimple fracture for both cases, the strain ageing model is coupled with a Rousselier model involving void growth. The flat fracture of the sample at room temperature and the associated macroscopic curve is reproduced successfully, but the fracture energy at elevated temperature is overestimated and the slant fracture is not reproduced. This underlines the importance of studying further the impact of the Portevin–Le Chatelier effect on failure to enhance the predictive capabilities of modelling approaches.

CRedit authorship contribution statement

S.C. Ren: Investigation, Conceptualization, Methodology, Formal analysis, Data curation, Software, Writing - original draft, Writing - review & editing. **T.F. Morgeneyer:** Investigation, Conceptualization, Methodology, Writing - original draft, Writing - review & editing, Supervision, Project administration, Funding acquisition. **M. Mazière:** Methodology, Software, Supervision, Project administration. **S. Forest:** Conceptualization, Methodology, Supervision, Project administration, Writing - original draft, Writing - review & editing. **G. Rousselier:** Conceptualization, Methodology, Supervision, Writing - original draft, Writing - review & editing.

Declaration of competing interest

The authors declare that they have no known competing financial interests or personal relationships that could have appeared to influence the work reported in this paper.

Acknowledgements

The authors gratefully acknowledge EDF (thanks to Aurore Parrot and Patrick Le Delliou) for material supply. Institut Carnot M.I.N.E.S is thanked for some funding.

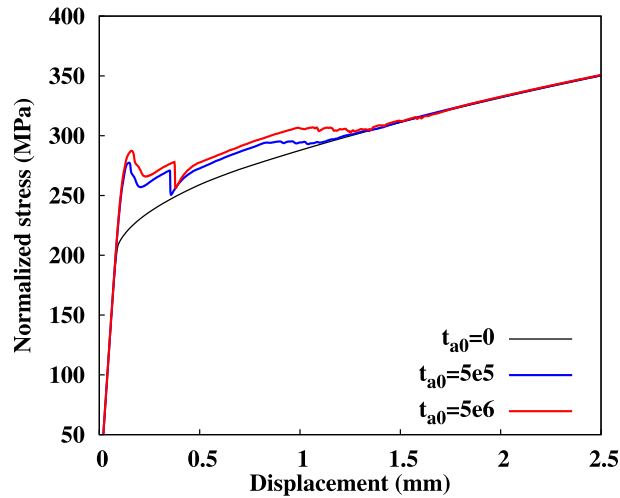


Fig. A.19. Comparison of the FEM simulation results with and without Lüders effect for SENT tests.

Appendix. Simulations of non-symmetric conditions during SENT tearing test

The full 3D simulations performed here shed light on the information needed to determine the range of Lüders effect in such a specimen geometry. Fig. A.19 gives a comparison between the simulation results without Lüders effect and involving Lüders effect by adjusting t_{a0} . The Lüders phenomenon only affects a limited portion of the stress–strain curve and always ends with a stress plateau (or stress drop). This effect has not been mentioned in Han et al. (2011) although a small stress plateau is visible on their global stress curve. The simulations also reproduced the yield peak, however the shape is too sharp compared with experiments (see Fig. A.19). This discrepancy could be due to slight out of plane displacement during the experiments. The objective of this appendix is to investigate the effect of perturbations of boundary conditions on the shape of the macroscopic curve. Three possible perturbation modes are simulated during the test, see respectively Sections Appendices A.2, A.3, A.4 and Figs. A.20, A.21 and A.22. The mode III loading turns out to have a significant influence on the shape of Lüders peak and results in a more realistic overall curve, see Appendix A.4.

The amplitude of PLC serrations in the current simulations is less than PLC experimental results. This is due to the fact that the current simulations did not take into account the influence of the testing machine stiffness on the PLC effect. As shown in Wang et al. (2012), incorporating machine stiffness into the model gives a more realistic amplitude of PLC serrations.

A.1. Lüders plateau controlled by initial ageing time t_{a0}

Firstly, the Lüders effect is studied numerically in order to determine its influence on the overall hardening. The Lüders effect in the current SENT specimen is not characterized by a well-defined stress plateau in contrast to the tensile tests. Fig. A.19 compares the result by artificially deactivating the Lüders effect ($t_{a0} = 0$ s) with that showing Lüders effect. With the Lüders effect ($t_{a0} \neq 0$ s), an over hardening is observed after the yield point followed by a stress plateau. The influence of initial ageing time on the over hardening by Lüders effect is presented in Fig. A.19. A longer initial ageing time results in a larger range of Lüders effect on the stress–displacement curve.

This simulation result confirms the characteristics of Lüders effect in such a specimen geometry. In the following simulations, t_{a0} is set to be 10^4 s for 175 °C and 5×10^6 s for 20 °C. These values are obtained by comparing them with experimental curves in the current work.

A.2. The effect of torsion due to grip misalignment

The out-of-plane displacement can be checked by DIC. Fig. A.20 shows the torsion movement after closing the grips. A very slight torsion induced z -direction displacement around $30 \mu\text{m}$ and could be found to be due to grip misalignment.

The influence of this out-of-plane movement has been investigated numerically. An initial relative rotation of $\pm 0.24^\circ$ is applied to the upper and lower surfaces (see Fig. A.20). The simulated out-of-plane displacement component u_z field after initial rotation is close to DIC measurements. A comparison of the stress–displacement curves of pure mode I loading and that with a slight torsion is presented in Fig. A.20. Only a slight change of the Lüders yield peak can be seen.

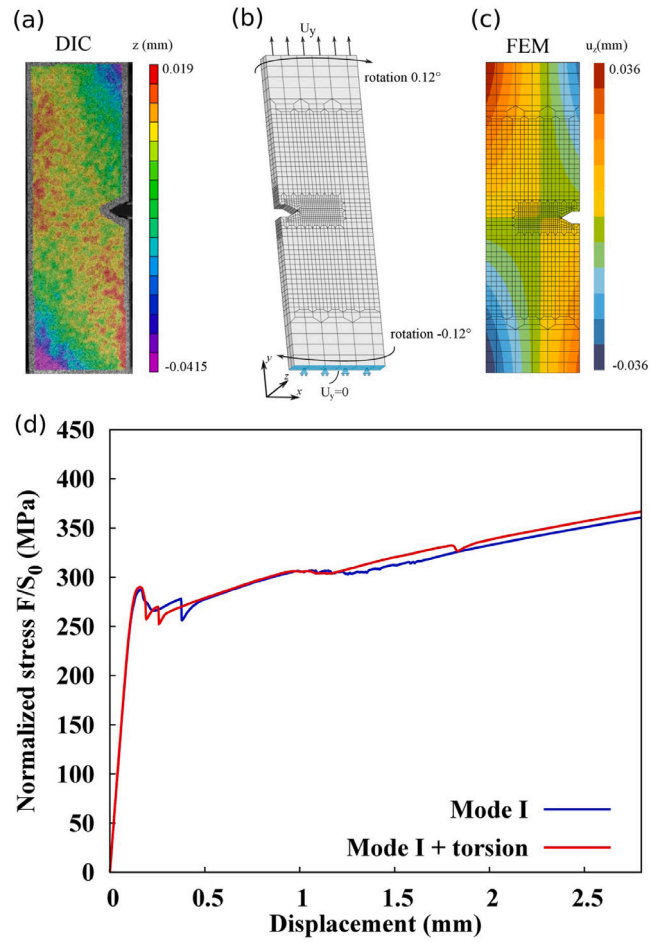


Fig. A.20. Influence of torsion due to grip misalignment: (a) Out-of-plane rotation measured by DIC; (b) Corresponding simulation boundary conditions; (c) u_x displacement field after torsion by FEM simulation; (d) Comparison of stress–displacement curves with mode I loading and with additional torsion.

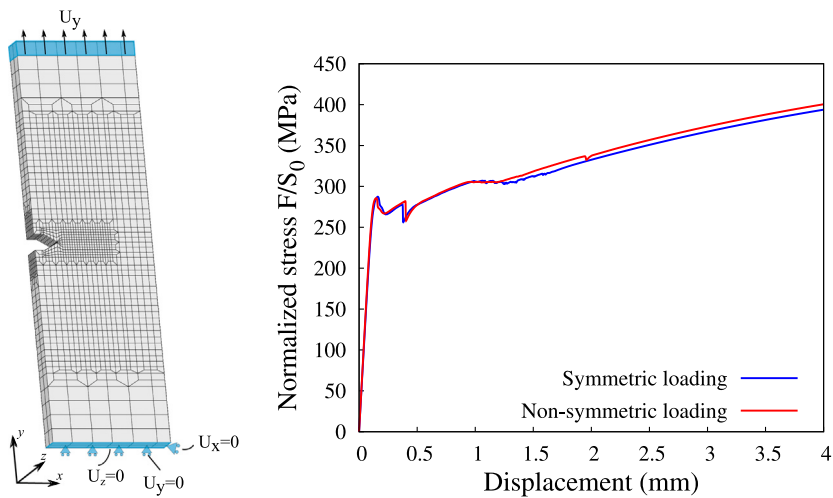


Fig. A.21. FEM simulation of non-symmetrical loading.

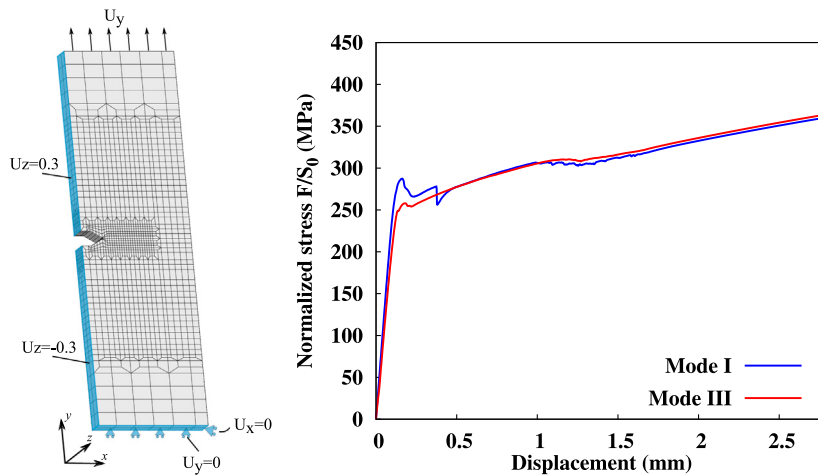


Fig. A.22. FEM simulation of mode III loading.

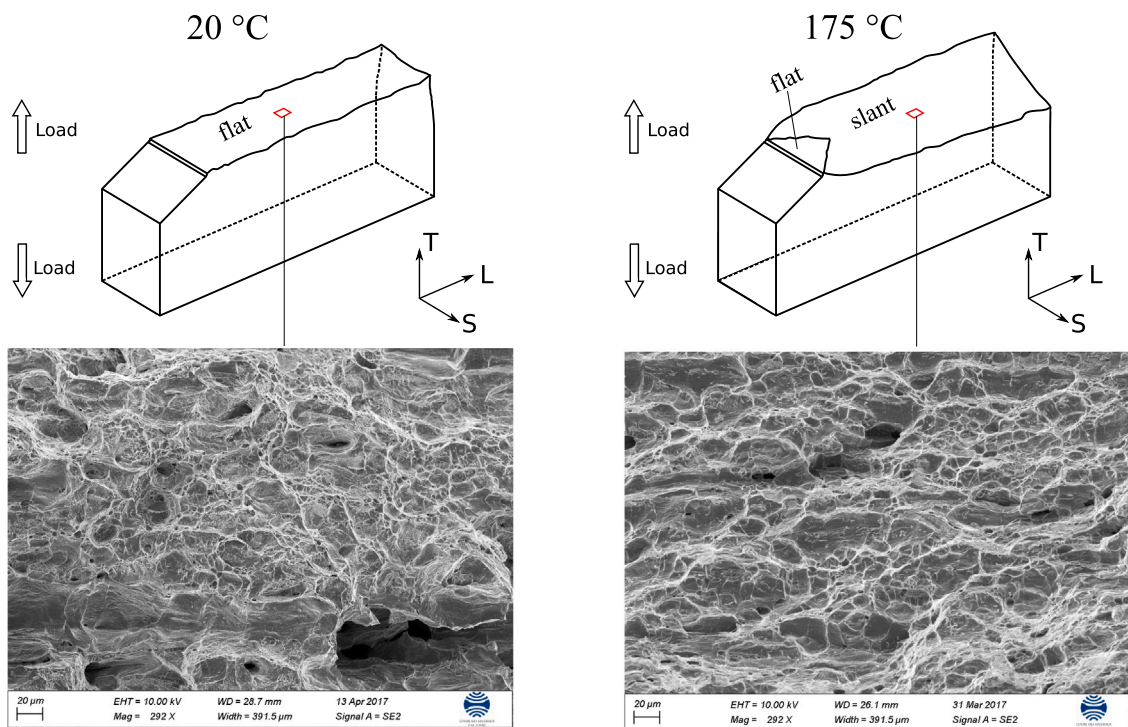


Fig. A.23. Comparison of the SEM fractography of specimens tested at 20 °C and 175 °C with a loading rate of 0.01 mm/s.

A.3. The effect of non-symmetrical loading

According to experimental measurements, the length of the section clamped inside the grip could vary from 1 mm to 3 mm when mounting specimens. We tested the influence of this non-symmetrical loading by eliminating one layer of elements on the top (~3.5 mm shorter on the upper side). Fig. A.21 gives the simulated stress–displacement curve which showed negligible influence of non-symmetrical loading.

A.4. The effect of mode III loading

Another numerical test is carried out by applying mode III loading. A perturbation displacement of 0.3 mm is applied on the specimen for simulating a typical misalignment of loading fixtures. Fig. A.22 shows the schematics of boundary conditions and the

stress–displacement curve. It can be seen that this mode of loading has a significant influence on the initial yield peak. The shape of mode III loading curve is more realistic than that of pure mode I loading.

A.5. SEM fractographs at 20 °C and 175 °C

The fractography studies at the microscopic level are carried out on these SENT specimens using a ZEISS DSM982 scanning electron microscope (SEM). Fig. A.23 compares the SEM fracto graphs of the specimens tested at 20 °C and 175 °C. Spherical dimples can be observed in both cases. A very slight shearing effect can be noticed in these slant areas for the specimen tested at 175 °C.

References

- Ait-Amokhtar, H., Fressengeas, C., Boudrahem, S., 2008. The dynamics of Portevin–Le Chatelier bands in an Al–Mg alloy from infrared thermography. *Mater. Sci. Eng. A* 488 (1), 540–546. <http://dx.doi.org/10.1016/j.msea.2007.11.075>, URL <http://www.sciencedirect.com/science/article/pii/S0921509307018631>.
- Ait-Amokhtar, H., Vacher, P., Boudrahem, S., 2006. Kinematics fields and spatial activity of Portevin–Le Chatelier bands using the digital image correlation method. *Acta Mater.* 54 (16), 4365–4371. <http://dx.doi.org/10.1016/j.actamat.2006.05.028>, URL <http://www.sciencedirect.com/science/article/pii/S1359645406003697>.
- Amar, E., Pineau, A., 1985. Interpretation of ductile fracture toughness temperature dependence of a low strength steel in terms of a local approach. *Eng. Fract. Mech.* 22 (6), 1061–1071. [http://dx.doi.org/10.1016/0013-7944\(85\)90044-X](http://dx.doi.org/10.1016/0013-7944(85)90044-X), URL <http://www.sciencedirect.com/science/article/pii/001379448590044X>.
- Beardmore, D., da Fonseca, J.Q., Romero, J., English, C., Ortner, S., Sharples, J., Sherry, A., Wilkes, M., 2013. Study of Lüders phenomena in reactor pressure vessel steels. *Mater. Sci. Eng. A* 588, 151–166. <http://dx.doi.org/10.1016/j.msea.2013.05.021>, URL <http://www.sciencedirect.com/science/article/pii/S0921509313005510>.
- Belotteau, J., 2009. Behavior and Rupture of a C–Mn Steel in the Presence of Aging Under Strain (Ph.D. thesis). (2009ECAP0002), Ecole Centrale Paris.
- Belotteau, J., Berdin, C., Forest, S., Parrot, A., Prioul, C., 2009. Mechanical behavior and crack tip plasticity of a strain aging sensitive steel. *Mater. Sci. Eng. A* 526 (1), 156–165. <http://dx.doi.org/10.1016/j.msea.2009.07.013>, URL <http://www.sciencedirect.com/science/article/pii/S0921509309007722>.
- Benallal, A., Berstad, T., Børvik, T., Clausen, A., Hopperstad, O., 2006. Dynamic strain aging and related instabilities: experimental, theoretical and numerical aspects. *Eur. J. Mech. A Solids* 25 (3), 397–424. <http://dx.doi.org/10.1016/j.euromechsol.2005.10.007>, URL <http://www.sciencedirect.com/science/article/pii/S0997753805001440>.
- Benallal, A., Berstad, T., Børvik, T., Hopperstad, O., Koutiri, I., De Codes, R.N., 2008. An experimental and numerical investigation of the behaviour of AA5083 aluminium alloy in presence of the Portevin–Le Chatelier effect. *Int. J. Plast.* 24 (10), 1916–1945. <http://dx.doi.org/10.1016/j.ijplas.2008.03.008>, URL <http://www.sciencedirect.com/science/article/pii/S0749641908000570>.
- Besnard, G., Hild, F., Roux, S., 2006. Finite-element displacement fields analysis from digital images: application to Portevin–Le Chatelier bands. *Exp. Mech.* 46 (6), 789–803. <http://dx.doi.org/10.1007/s11340-006-9824-8>.
- Besson, J., Cailletaud, G., Chaboche, J., Forest, S., 2009. Non-Linear Mechanics of Materials, Vol. 167. Springer, <http://dx.doi.org/10.1007/978-90-481-3356-7>.
- van den Beukel, A., 1975. Theory of the effect of dynamic strain aging on mechanical properties. *Phys. Status Solidi* 30 (1), 197–206. <http://dx.doi.org/10.1002/pssa.2210300120>, URL <https://onlinelibrary.wiley.com/doi/abs/10.1002/pssa.2210300120>.
- Böhlke, T., Bondár, G., Estrin, Y., Lebyodkin, M.A., 2009. Geometrically non-linear modeling of the Portevin–Le Chatelier effect. *Comput. Mater. Sci.* 44 (4), 1076–1088. <http://dx.doi.org/10.1016/j.commatsci.2008.07.036>, URL <http://www.sciencedirect.com/science/article/pii/S0927025608003601>.
- Brechet, Y., Estrin, Y., 1996. Pseudo-Portevin–Le Chatelier effect in ordered alloys. *Scr. Mater.* 35 (2), 217–223. [http://dx.doi.org/10.1016/1359-6462\(96\)00126-1](http://dx.doi.org/10.1016/1359-6462(96)00126-1).
- Buirette, C., Huez, J., Gey, N., Vassel, A., Andrieu, E., 2014. Study of crack propagation mechanisms during Charpy impact toughness tests on both equiaxed and lamellar microstructures of Ti–6Al–4V titanium alloy. *Mater. Sci. Eng. A* 618, 546–557. <http://dx.doi.org/10.1016/j.msea.2014.09.048>, URL <http://www.sciencedirect.com/science/article/pii/S0921509314011538>.
- Buljac, A., Hild, F., Helfen, L., Morgeneyer, T.F., 2018. On deformation and damage micromechanisms in strong work hardening 2198 T3 aluminium alloy. *Acta Mater.* 149, 29–45. <http://dx.doi.org/10.1016/j.actamat.2018.01.026>, URL <http://www.sciencedirect.com/science/article/pii/S1359645418300570>.
- Buljac, A., Taillandier-Thomas, T., Morgeneyer, T.F., Helfen, L., Roux, S., Hild, F., 2016. Slant strained band development during flat to slant crack transition in AA2198 T8 sheet: in situ 3D measurements. *Int. J. Fract.* 200 (1–2), 49–62. <http://dx.doi.org/10.1007/s10704-015-0052-z>.
- Cai, Y., Tian, C., Zhang, G., Han, G., Yang, S., Fu, S., Cui, C., Zhang, Q., 2017. Influence of γ precipitates on the critical strain and localized deformation of serrated flow in Ni-based superalloys. *J. Alloys Compd.* 690, 707–715. <http://dx.doi.org/10.1016/j.jallcom.2016.08.194>, URL <http://www.sciencedirect.com/science/article/pii/S0925838816325737>.
- Cai, Y., Yang, S., Wang, Y., Fu, S., Zhang, Q., 2016. Characterization of the deformation behaviors associated with the serrated flow of a 5456 Al-based alloy using two orthogonal digital image correlation systems. *Mater. Sci. Eng. A* 664, 155–164. <http://dx.doi.org/10.1016/j.msea.2016.04.003>, URL <http://www.sciencedirect.com/science/article/pii/S0921509316303641>.
- Casarotto, L., Dierke, H., Tutsch, R., Neuhäuser, H., 2009. On nucleation and propagation of PLC bands in an Al–3Mg alloy. *Mater. Sci. Eng. A* 527 (1), 132–140. <http://dx.doi.org/10.1016/j.msea.2009.07.043>, URL <http://www.sciencedirect.com/science/article/pii/S0921509309008181>.
- Chaboche, J., Gaubert, A., Kanoute, P., Longuet, A., Azzouz, F., Mazière, M., 2013. Viscoplastic constitutive equations of combustion chamber materials including cyclic hardening and dynamic strain aging. *Int. J. Plast.* 46, 1–22. <http://dx.doi.org/10.1016/j.ijplas.2012.09.011>.
- Chakravartty, J., Wadekar, S., Sinha, T., Asundi, M., 1983. Dynamic strain-ageing of A203D nuclear structural steel. *J. Nuclear Mater.* 119 (1), 51–58. [http://dx.doi.org/10.1016/0022-3115\(83\)90051-X](http://dx.doi.org/10.1016/0022-3115(83)90051-X), URL <http://www.sciencedirect.com/science/article/pii/002231158390051X>.
- Cheng, T., Xu, X., Cai, Y., Fu, S., Gao, Y., Su, Y., Zhang, Y., Zhang, Q., 2015. Investigation of Portevin–Le Chatelier effect in 5456 Al-based alloy using digital image correlation. *Opt. Lasers Eng.* 65, 89–92. <http://dx.doi.org/10.1016/j.optlaseng.2014.06.012>, URL <http://www.sciencedirect.com/science/article/pii/S0143816614001572>.
- Chihab, K., Estrin, Y., Kubin, L., Vergnol, J., 1987. The kinetics of the portevin-le chatelier bands in an Al-5at% Mg alloy. *Scr. Metall.* 21 (2), 203–208. [http://dx.doi.org/10.1016/0036-9748\(87\)90435-2](http://dx.doi.org/10.1016/0036-9748(87)90435-2), URL <http://www.sciencedirect.com/science/article/pii/0036974887904352>.
- Chmelík, F., Pink, E., Król, J., Balík, J., Pešička, J., Lukáč, P., 1998. Mechanisms of serrated flow in aluminium alloys with precipitates investigated by acoustic emission. *Acta Mater.* 46 (12), 4435–4442. [http://dx.doi.org/10.1016/S1359-6454\(98\)00070-6](http://dx.doi.org/10.1016/S1359-6454(98)00070-6), URL <http://www.sciencedirect.com/science/article/pii/S1359645498000706>.
- Chmelík, F., Ziegenbein, A., Neuhäuser, H., Lukáč, P., 2002. Investigating the Portevin–Le Chatelier effect by the acoustic emission and laser extensometry techniques. *Mater. Sci. Eng. A* 324 (1), 200–207. [http://dx.doi.org/10.1016/S0921-5093\(01\)01312-0](http://dx.doi.org/10.1016/S0921-5093(01)01312-0), URL <http://www.sciencedirect.com/science/article/pii/S0921509301013120>.
- Clausen, A.H., Børvik, T., Hopperstad, O.S., Benallal, A., 2004. Flow and fracture characteristics of aluminium alloy AA5083–H116 as function of strain rate, temperature and triaxiality. *Mater. Sci. Eng. A* 364 (1), 260–272. <http://dx.doi.org/10.1016/j.msea.2003.08.027>, URL <http://www.sciencedirect.com/science/article/pii/S0921509303007032>.

- de Codes, R.N., Hopperstad, O., Engler, O., Lademo, O.-G., Embury, J., Benallal, A., 2011. Spatial and temporal characteristics of propagating deformation bands in AA5182 alloy at room temperature. *Metall. Mater. Trans. A* 42 (11), 3358–3369. <http://dx.doi.org/10.1007/s11661-011-0749-1>.
- Coër, J., Manach, P.Y., Laurent, H., Oliveira, M.C., Menezes, L.F., 2013. Piobert–Lüders plateau and Portevin–Le Chatelier effect in an Al–Mg alloy in simple shear. *Mech. Res. Commun.* 48, 1–7. <http://dx.doi.org/10.1016/j.mechrescom.2012.11.008>, URL <http://www.sciencedirect.com/science/article/pii/S0093641312001905>.
- Cottrell, A.H., Bilby, B.A., 1949. Dislocation theory of yielding and strain ageing of iron. *Proc. Phys. Soc. A* 62 (1), 49, URL <http://stacks.iop.org/0370-1298/62/i=1/a=308>.
- Curtin, W.A., Olmsted, D.L., Hector, L.G., 2006. A predictive mechanism for dynamic strain ageing in aluminium–magnesium alloys. *Nat. Mater.* 5 (11), 875–880. <http://dx.doi.org/10.1038/nmat1765>.
- Dalloz, A., 2007. Étude de l'endommagement par la découpe des aciers dual phase pour application automobile (Ph.D. thesis). École Nationale Supérieure des Mines de Paris.
- Dybiec, H., Chaturvedi, M.C., 1991. Serrated yielding in Inconel 718. *Arch. Metall.* 36 (3), 341–352.
- Epperly, E., Sills, R., 2020. Comparison of continuum and cross-core theories of dynamic strain aging. *J. Mech. Phys. Solids* 141, 103944. <http://dx.doi.org/10.1016/j.jmps.2020.103944>, URL <http://www.sciencedirect.com/science/article/pii/S0022509620301800>.
- Fournier, L., Delafosse, D., Magnin, T., 2001. Oxidation induced intergranular cracking and Portevin–Le Chatelier effect in nickel base superalloy 718. *Mater. Sci. Eng. A* 316 (1), 166–173. [http://dx.doi.org/10.1016/S0921-5093\(01\)01224-2](http://dx.doi.org/10.1016/S0921-5093(01)01224-2), URL <http://www.sciencedirect.com/science/article/pii/S0921509301012242>.
- Gomiero, P., Brechet, Y., Louchet, F., Tourabi, A., Wack, B., 1992. Microstructure and mechanical properties of a 2091 Al–Li–Cu–Mg alloy. *Acta Metall. Mater.* 40 (4), 863–871. [http://dx.doi.org/10.1016/0956-7151\(92\)90029-E](http://dx.doi.org/10.1016/0956-7151(92)90029-E), URL <http://www.sciencedirect.com/science/article/pii/095671519290029E>.
- Grabner, F., Österreicher, J.A., Gruber, B., Papenberg, N., Gerstner, F., Kirnstötter, S., Schlägl, C.M., 2019. Cryogenic forming of Al–Mg alloy sheet for car outer body applications. *Adv. Energy Mater.* 21 (8), 1900089. <http://dx.doi.org/10.1002/adem.201900089>, URL <https://onlinelibrary.wiley.com/doi/abs/10.1002/adem.201900089>.
- Graff, S., Dierke, H., Forest, S., Neuhäuser, H., Strudel, J.-L., 2008. Finite element simulations of the Portevin–Le Chatelier effect in metal–matrix composites. *Phil. Mag.* 88 (28–29), 3389–3414. <http://dx.doi.org/10.1080/14786430802108472>.
- Graff, S., Forest, S., Strudel, J.-L., Prioul, C., Pilvin, P., Béchade, J.-L., 2004. Strain localization phenomena associated with static and dynamic strain ageing in notched specimens: finite element simulations. *Mater. Sci. Eng. A* 387, 181–185. <http://dx.doi.org/10.1016/j.msea.2004.02.083>, URL <http://www.sciencedirect.com/science/article/pii/S0921509304004538>.
- Graff, S., Forest, S., Strudel, J.-L., Prioul, C., Pilvin, P., Béchade, J.-L., 2005. Finite element simulations of dynamic strain ageing effects at V-notches and crack tips. *Scr. Mater.* 52 (11), 1181–1186. <http://dx.doi.org/10.1016/j.scriptamat.2005.02.007>, URL <http://www.sciencedirect.com/science/article/pii/S1359646205000916>.
- Halim, H., Wilkinson, D.S., Niewczas, M., 2007. The portevin–le chatelier (PLC) effect and shear band formation in an AA5754 alloy. *Acta Mater.* 55 (12), 4151–4160. <http://dx.doi.org/10.1016/j.actamat.2007.03.007>, URL <http://www.sciencedirect.com/science/article/pii/S1359645407001917>.
- Han, Z., Luo, H., Wang, H., 2011. Effects of strain rate and notch on acoustic emission during the tensile deformation of a discontinuous yielding material. *Mater. Sci. Eng. A* 528 (13), 4372–4380. <http://dx.doi.org/10.1016/j.msea.2011.02.042>, URL <http://www.sciencedirect.com/science/article/pii/S0921509311002061>.
- Hickey, W.F., Ravi-Chandar, K., 2016. Transition from flat to slant fracture in ductile materials. In: *Recent Trends in Fracture and Damage Mechanics*. Springer, pp. 215–235. <http://dx.doi.org/10.1007/978-3-319-21467-2>.
- Huang, Z., Wagner, D., Bathias, C., 2015. Some metallurgical aspects of dynamic strain aging effect on the low cycle fatigue behavior of C–Mn steels. *Int. J. Fatigue* 80, 113–120. <http://dx.doi.org/10.1016/j.ijfatigue.2015.04.008>, URL <http://www.sciencedirect.com/science/article/pii/S0142112315001243>.
- Jiang, Z., Zhang, Q., Jiang, H., Chen, Z., Wu, X., 2005. Spatial characteristics of the Portevin–Le Chatelier deformation bands in Al–4at% Cu polycrystals. *Mater. Sci. Eng. A* 403 (1), 154–164. <http://dx.doi.org/10.1016/j.msea.2005.05.059>, URL <http://www.sciencedirect.com/science/article/pii/S0921509305004934>.
- Kim, K.-C., Kim, J.-T., Suk, J.-I., Sung, U.-H., Kwon, H.-K., 2004. Influences of the dynamic strain aging on the J–R fracture characteristics of the ferritic steels for reactor coolant piping system. *Nuclear Eng. Des.* 228 (1), 151–159. <http://dx.doi.org/10.1016/j.nucengdes.2003.06.014>, URL <http://www.sciencedirect.com/science/article/pii/S0029549303002887>.
- Klusemann, B., Fischer, G., Böhlke, T., Svendsen, B., 2015. Thermomechanical characterization of Portevin–Le Chatelier bands in AlMg3 (AA5754) and modeling based on a modified Estrin–McCormick approach. *Int. J. Plast.* 67, 192–216. <http://dx.doi.org/10.1016/j.ijplas.2014.10.011>, URL <http://www.sciencedirect.com/science/article/pii/S074964191400206X>.
- Kubin, L., Estrin, Y., 1984. Thermal effects in low-temperature deformation: The response to strain rate changes. *Cryst. Res. Technol.* 19 (6), 853–862. <http://dx.doi.org/10.1002/crat.2170190619>, URL <https://onlinelibrary.wiley.com/doi/abs/10.1002/crat.2170190619>.
- Kubin, L., Estrin, Y., 1985. The Portevin–Le Chatelier effect in deformation with constant stress rate. *Acta Metall.* 33 (3), 397–407. [http://dx.doi.org/10.1016/0001-6160\(85\)90082-3](http://dx.doi.org/10.1016/0001-6160(85)90082-3), URL <http://www.sciencedirect.com/science/article/pii/0001616085900823>.
- Le Cam, J.-B., Robin, E., Leotoing, L., Guines, D., 2017. Calorimetric analysis of Portevin–Le Chatelier bands under equibiaxial loading conditions in Al–Mg alloys: Kinematics and mechanical dissipation. *Mech. Mater.* 105, 80–88. <http://dx.doi.org/10.1016/j.mechmat.2016.11.012>, URL <http://www.sciencedirect.com/science/article/pii/S0167663616301272>.
- Marais, A., Mazière, M., Forest, S., Parrot, A., Le Delliou, P., 2012. Identification of a strain-aging model accounting for Lüders behavior in a C–Mn steel. *Phil. Mag.* 92 (28–30), 3589–3617. <http://dx.doi.org/10.1080/14786435.2012.699687>.
- Marchenko, M., Mazière, M., Forest, S., Strudel, J.L., 2016. Crystal plasticity simulation of strain aging phenomena in alpha-titanium at room temperature. *Int. J. Plast.* 85, 1–33. <http://dx.doi.org/10.1016/j.ijplas.2016.05.007>.
- Mazière, M., Besson, J., Forest, S., Tanguy, B., Chalons, H., Vogel, F., 2010. Numerical aspects in the finite element simulation of the Portevin–Le Chatelier effect. *Comput. Methods Appl. Mech. Engrg.* 199 (9), 734–754. <http://dx.doi.org/10.1016/j.cma.2009.11.004>, URL <http://www.sciencedirect.com/science/article/pii/S004578250900379X>.
- Mazière, M., Dierke, H., 2012. Investigations on the Portevin–Le Chatelier critical strain in an aluminum alloy. *Comput. Mater. Sci.* 52 (1), 68–72. <http://dx.doi.org/10.1016/j.commatsci.2011.05.039>, URL <http://www.sciencedirect.com/science/article/pii/S0927025611003120>.
- Mazière, M., Pujol d'Andrebo, Q., 2015. Portevin–Le Chatelier effect under cyclic loading: experimental and numerical investigations. *Phil. Mag.* 95 (28–30), 3257–3277. <http://dx.doi.org/10.1080/14786435.2015.1049236>.
- McCormick, P.G., 1988. Theory of flow localisation due to dynamic strain ageing. *Acta Metall.* 36 (12), 3061–3067. [http://dx.doi.org/10.1016/0001-6160\(88\)90043-0](http://dx.doi.org/10.1016/0001-6160(88)90043-0), URL <http://www.sciencedirect.com/science/article/pii/0001616088900430>.
- Mesarovic, S.D., 1995. Dynamic strain aging and plastic instabilities. *J. Mech. Phys. Solids* 43 (5), 671–700. [http://dx.doi.org/10.1016/0022-5096\(95\)00010-G](http://dx.doi.org/10.1016/0022-5096(95)00010-G), URL <http://www.sciencedirect.com/science/article/pii/002250969500010G>.
- Min, J., Hector, L.G., Carsley, J.E., Stoughton, T.B., Carlson, B.E., Lin, J., 2015. Spatio-temporal characteristics of plastic instability in AA5182-O during biaxial deformation. *Mater. Des.* 83, 786–794. <http://dx.doi.org/10.1016/j.matdes.2015.06.039>, URL <http://www.sciencedirect.com/science/article/pii/S0264127515003895>.
- Min, J., Hector Jr, L.G., Zhang, L., Sun, L., Carsley, J.E., Lin, J., 2016. Plastic instability at elevated temperatures in a TRIP-assisted steel. *Mater. Des.* 95, 370–386. <http://dx.doi.org/10.1016/j.matdes.2016.01.113>, URL <http://www.sciencedirect.com/science/article/pii/S0264127516301113>.

- Morgeneyer, T.F., Taillandier-Thomas, T., Buljac, A., Helfen, L., cois Hild, F., 2016. On strain and damage interactions during tearing: 3D in situ measurements and simulations for a ductile alloy (AA2139-T3). *J. Mech. Phys. Solids* 96, 550–571. <http://dx.doi.org/10.1016/j.jmps.2016.07.012>, URL <http://www.sciencedirect.com/science/article/pii/S0022509615301861>.
- Morgeneyer, T.F., Taillandier-Thomas, T., Helfen, L., Baumbach, T., Sinclair, I., Roux, S., Hild, F., 2014. In situ 3-D observation of early strain localization during failure of thin Al alloy (2198) sheet. *Acta Mater.* 69, 78–91. <http://dx.doi.org/10.1016/j.actamat.2014.01.033>, URL <http://www.sciencedirect.com/science/article/pii/S1359645414000500>.
- Mulfrod, R., Kocks, U., 1979. New observations on the mechanisms of dynamic strain aging and of jerky flow. *Acta Metall.* 27 (7), 1125–1134. [http://dx.doi.org/10.1016/0001-6160\(79\)90130-5](http://dx.doi.org/10.1016/0001-6160(79)90130-5), URL <http://www.sciencedirect.com/science/article/pii/0001616079901305>.
- Nogueira De Codes, R., Benallal, A., 2011. Influence of specimen geometry on the Portevin–Le Châtelier effect due to dynamic strain aging for the AA5083-H116 aluminum alloy. *J. Mech. Mater. Struct.* 6 (7), 951–968. <http://dx.doi.org/10.2140/jomms.2011.6.951>.
- Penning, P., 1972. Mathematics of the Portevin–Le Châtelier effect. *Acta Metall.* 20 (10), 1169–1175. [http://dx.doi.org/10.1016/0001-6160\(72\)90165-4](http://dx.doi.org/10.1016/0001-6160(72)90165-4), URL <http://www.sciencedirect.com/science/article/pii/0001616072901654>.
- Prasad, K., Varma, V.K., 2008. Serrated flow behavior in a near alpha titanium alloy IMI 834. *Mater. Sci. Eng. A* 486 (1), 158–166. <http://dx.doi.org/10.1016/j.msea.2007.09.020>, URL <http://www.sciencedirect.com/science/article/pii/S0921509307016437>.
- Ranc, N., Du, W., Ranc, I., Wagner, D., 2016. Experimental studies of Portevin–Le Châtelier plastic instabilities in carbon-manganese steels by infrared pyrometry. *Mater. Sci. Eng. A* 663, 166–173. <http://dx.doi.org/10.1016/j.msea.2016.03.096>, URL <http://www.sciencedirect.com/science/article/pii/S0921509316303082>.
- Ranc, N., Wagner, D., 2005. Some aspects of Portevin–Le Châtelier plastic instabilities investigated by infrared pyrometry. *Mater. Sci. Eng. A* 394 (1), 87–95. <http://dx.doi.org/10.1016/j.msea.2004.11.042>, URL <http://www.sciencedirect.com/science/article/pii/S0921509304013656>.
- Rao, K.B.S., Kalluri, S., Halford, G.R., McGaw, M.A., 1995. Serrated flow and deformation substructure at room temperature in Inconel 718 superalloy during strain controlled fatigue. *Scr. Metall. Mater.* 32 (4), 493–498. [http://dx.doi.org/10.1016/0956-716X\(95\)90826-6](http://dx.doi.org/10.1016/0956-716X(95)90826-6).
- Ren, S., Mazière, M., Forest, S., Morgeneyer, T.F., Rousselier, G., 2017. A constitutive model accounting for strain ageing effects on work-hardening. Application to a C–Mn steel. *C. R. Mécanique* 345 (12), 908–921. <http://dx.doi.org/10.1016/j.crme.2017.09.005>, URL <http://www.sciencedirect.com/science/article/pii/S1631072117301900>.
- Ren, S., Morgeneyer, T.F., Mazière, M., Forest, S., Rousselier, G., 2019. Portevin-Le Châtelier effect triggered by complex loading paths in an Al–Cu aluminium alloy. *Phil. Mag.* 99 (6), 659–678. <http://dx.doi.org/10.1080/14786435.2018.1550296>.
- Rousselier, G., 1987. Ductile fracture models and their potential in local approach of fracture. *Nucl. Eng. Des.* 105 (1), 97–111. [http://dx.doi.org/10.1016/0029-5493\(87\)90234-2](http://dx.doi.org/10.1016/0029-5493(87)90234-2), URL <http://www.sciencedirect.com/science/article/pii/0029549387902342>.
- Rousselier, G., 2001. Dissipation in porous metal plasticity and ductile fracture. *J. Mech. Phys. Solids* 49 (8), 1727–1746. [http://dx.doi.org/10.1016/S0022-5096\(01\)00013-8](http://dx.doi.org/10.1016/S0022-5096(01)00013-8), URL <http://www.sciencedirect.com/science/article/pii/S0022509601000138>.
- Rousselier, G., Morgeneyer, T.F., Ren, S., Mazière, M., Forest, S., 2017. Interaction of the Portevin–Le Châtelier phenomenon with ductile fracture of a thin aluminium CT specimen: experiments and simulations. *Int. J. Fract.* 206 (1), 95–122. <http://dx.doi.org/10.1007/s10704-017-0203-5>.
- Rousselier, G., Quilici, S., 2015. Combining porous plasticity with Coulomb and Portevin-Le Châtelier models for ductile fracture analyses. *Int. J. Plast.* 69, 118–133. <http://dx.doi.org/10.1016/j.ijplas.2015.02.008>, URL <http://www.sciencedirect.com/science/article/pii/S0749641915000388>.
- Simonsen, B.C., Törnqvist, R., 2004. Experimental and numerical modelling of ductile crack propagation in large-scale shell structures. *Mar. Struct.* 17 (1), 1–27. <http://dx.doi.org/10.1016/j.marstruc.2004.03.004>, URL <http://www.sciencedirect.com/science/article/pii/S0951833904000334>.
- Sutton, M.A., 2008. Digital image correlation for shape and deformation measurements. In: *Springer Handbook of Experimental Solid Mechanics*. Springer, pp. 565–600. http://dx.doi.org/10.1007/978-0-387-30877-7_20.
- Swaminathan, B., Abuzaid, W., Sehitoğlu, H., Lambros, J., 2015. Investigation using digital image correlation of Portevin-Le Châtelier effect in Hastelloy X under thermo-mechanical loading. *Int. J. Plast.* 64, 177–192. <http://dx.doi.org/10.1016/j.ijplas.2014.09.001>, URL <http://www.sciencedirect.com/science/article/pii/S0749641914001855>.
- Tong, W., Tao, H., Zhang, N., Hector, L.G., 2005. Time-resolved strain mapping measurements of individual Portevin–Le Châtelier deformation bands. *Scr. Mater.* 53 (1), 87–92. <http://dx.doi.org/10.1016/j.scriptamat.2005.03.020>, URL <http://www.sciencedirect.com/science/article/pii/S135964620500151X>.
- Wagner, D., Roubier, N., Prioul, C., 2006. Measurement of sensitivity to dynamic strain aging in C–Mn steels by internal friction experiments. *Mater. Sci. Technol.* 22 (3), 301–307. <http://dx.doi.org/10.1179/174328406X86155>.
- Wang, H., 2011. *Mechanical Behavior and Fracture of the C-Mn Steels in the Presence of Dynamic Strain Aging* (Ph.D. thesis). (2011ECAP0022), Ecole Centrale Paris.
- Wang, H., Berdin, C., Mazière, M., Forest, S., Prioul, C., Parrot, A., Le-Delliou, P., 2011. Portevin–Le Châtelier (PLC) instabilities and slant fracture in C-Mn steel round tensile specimens. *Scr. Mater.* 64, 430–433.
- Wang, H., Berdin, C., Mazière, M., Forest, S., Prioul, C., Parrot, A., Le-Delliou, P., 2012. Experimental and numerical study of dynamic strain ageing and its relation to ductile fracture of a C–Mn steel. *Mater. Sci. Eng. A* 547, 19–31. <http://dx.doi.org/10.1016/j.msea.2012.03.069>, URL <http://www.sciencedirect.com/science/article/pii/S092150931200439X>.
- Wenman, M., Chard-Tuckey, P., 2010. Modelling and experimental characterisation of the Lüders strain in complex loaded ferritic steel compact tension specimens. *Int. J. Plast.* 26 (7), 1013–1028. <http://dx.doi.org/10.1016/j.ijplas.2009.12.005>, URL <http://www.sciencedirect.com/science/article/pii/S0749641909001661>.
- Xiao, Y., Zeng, P., Lei, L., 2016. Effect of double-edge semi-circular notches on the mechanical response of superelastic NiTi shape memory alloy: Experimental observations. *J. Strain Anal. Eng. Des.* 51 (8), 555–562. <http://dx.doi.org/10.1177/0309324716661460>.
- Xue, L., Wierzbicki, T., 2009. Numerical simulation of fracture mode transition in ductile plates. *Int. J. Solids Struct.* 46 (6), 1423–1435. <http://dx.doi.org/10.1016/j.ijsolstr.2008.11.009>, URL <http://www.sciencedirect.com/science/article/pii/S0020768308004836>.
- Yuzbekova, D., Mogucheva, A., Zhemchuzhnikova, D., Lebedkina, T., Lebyodkin, M., Kaibyshev, R., 2017. Effect of microstructure on continuous propagation of the Portevin-Le Châtelier deformation bands. *Int. J. Plast.* 96, 210–226. <http://dx.doi.org/10.1016/j.ijplas.2017.05.004>, URL <http://www.sciencedirect.com/science/article/pii/S0749641917300165>.
- Zavattieri, P., Savic, V., Hector, L., Fekete, J., Tong, W., Xuan, Y., 2009. Spatio-temporal characteristics of the Portevin–Le Châtelier effect in austenitic steel with twinning induced plasticity. *Int. J. Plast.* 25 (12), 2298–2330. <http://dx.doi.org/10.1016/j.ijplas.2009.02.008>, URL <http://www.sciencedirect.com/science/article/pii/S0749641909000266>.
- Zdunek, J., Brynk, T., Mizera, J., Pakiela, Z., Kurzydowski, K.J., 2008. Digital Image Correlation investigation of Portevin–Le Châtelier effect in an aluminium alloy. *Mater. Charact.* 59 (10), 1429–1433. <http://dx.doi.org/10.1016/j.matchar.2008.01.004>, URL <http://www.sciencedirect.com/science/article/pii/S1044580308000272>.
- Zhang, Q., Jiang, Z., Jiang, H., Chen, Z., Wu, X., 2005. On the propagation and pulsation of Portevin-Le Châtelier deformation bands: An experimental study with digital speckle pattern metrology. *Int. J. Plast.* 21 (11), 2150–2173. <http://dx.doi.org/10.1016/j.ijplas.2005.03.017>, URL <http://www.sciencedirect.com/science/article/pii/S0749641905000811>.
- Zhang, S., McCormick, P., Estrin, Y., 2001. The morphology of Portevin–Le Châtelier bands: finite element simulation for Al–Mg–Si. *Acta Mater.* 49 (6), 1087–1094. [http://dx.doi.org/10.1016/S1359-6454\(00\)00380-3](http://dx.doi.org/10.1016/S1359-6454(00)00380-3), URL <http://www.sciencedirect.com/science/article/pii/S1359645400003803>.